Original Article

Composite alkali-activated materials with waste tire rubber designed for additive manufacturing: an eco-sustainable and energy saving approach

Marco Valente [a,b,*], *Matteo Sambucci* [a,b], *Mehdi Chougan* [c], *Seyed Hamidreza Ghaffar* [c,d]

[a] *Department of Chemical Engineering, Materials, Environment, Sapienza University of Rome, 00184, Rome, Italy*
[b] *INSTM Reference Laboratory for Engineering of Surface Treatments, UdR Rome, Sapienza University of Rome, 00184, Rome, Italy*
[c] *Department of Civil and Environmental Engineering, Brunel University, London, Uxbridge, Middlesex, UB 8 3PH, United Kingdom*
[d] *Applied Science Research Center, Applied Science Private University, Jordan*

ARTICLE INFO

ABSTRACT

There is an increasing trend in research projects and case studies to demonstrate the potential of Additive Manufacturing (AM) with concrete, better known as 3D concrete printing. Like ordinary construction, the latest upgrades on this topic are strongly focused towards improving eco-sustainability in terms of low-carbon materials. Low-carbon binders' alternative to Portland cement and the utilisation of selected waste materials in place to virgin aggregates has high potential in fulfilling the sustainable development goals. In this paper, an experimental study was performed by incorporating ground waste tire rubber aggregates of different size gradation (0−1 mm and 1−3 mm) and replacement levels (50 v/v% and 100 v/v%) in a "greener" alkali-activated mix designed for 3D printing applications. First, the experimental program involved the optimization of mix design rheology and printing parameters to successfully integrate rubber aggregates into the printable alkali-activated mixtures. Then, a comprehensive characterization, including static mechanical testing, dynamic thermo-mechanical analysis, thermal conductivity testing, and acoustic insulation measurements was conducted. Comparison with identical Portland-based rubberized formulations designed for AM revealed better mechanical isotropy, flexural strength, thermo-mechanical behaviour, heat insulation, and high-frequency acoustic insulation for alkali-activated composites. The influence of rubber aggregate size on the fresh and hardened state behaviour of the mixes was also studied and discussed. Keeping the losses in mechanical strength restrained, the rubberized composites designed in this study have demonstrated significant thermal and acoustic insulation properties that are desired for energy-saving applications in buildings. The research verified the practicability of using waste aggregates in low-carbon binders for sustainable lightweight and thermo-acoustically effective applications, establishing an

---

* Corresponding author.
E-mail address: marco.valente@uniroma1.it (M. Valente).

attractive starting point to address future research on material optimization for practical purposes.

1.   Introduction

Digitalizing the fabrication processes in the construction industry is one of the pillars of the modern concept of Industry 4.0, which is recognized as a new technological era for manufacturing that uses cyber-physical systems, robotics, Internet of Things (IoT), Data and Services to connect production technologies with smart production processes [1]. The insertion of Industry 4.0 technologies helps construction industry to face the environmental challenges, identifying the strategies and new opportunities to become more sustainable [2].

In recent years, AM technology, better known as 3D printing, has gained broad attention in many industrial sectors such as tooling, automotive, aerospace, biomedical, food, digital art, and architectural design because it provides faster, easier, and less expensive solutions, as well as the ability to build a variety of complicated configurations that must overlap many traditional production processes. The key advantages of 3D printing are design freedom, design customization, waste reduction, the capacity to build complex structures, and rapid prototyping [3].

Recently, AM is attracting a growing interest in construction industry as well, especially in the concrete technology. The interest in exploiting 3D printing technologies in construction industry is mainly the result of the expectation of new freedom in terms of the design of shapes, elements, and structures, enabling new aesthetic and functional features (*freeform construction*). Architectural designers were often forced to use multiple identical elements in a project to save materials and reduce costs related the labor and the molds fabrication. AM is expected to revolutionize this paradigm, allowing designers to make each component unique without incurring prohibitive costs. Other advantages of this automated process are also expected, such as the reduction in construction time and expenses, greater worker safety, better quality and reliability, the saving of materials and, consequently, sustainability [4]. Within this context, the building sector is responsible for up to 33% of all emissions, around 40% of all material consumption, and 40% of all waste. Amid continued growth of the building stock, therefore, the pursuit for a greener and technologically advanced construction sector is dominating which aims to promote a resource-efficient and carbon-neutral built environment with accompanying socioeconomic benefits [5].

Extrusion-based concrete 3D printing (EC3DP) has been extensively researched and implemented by several academic teams and companies over the last twenty years [6,7]. A motion system (gantry or robotic arm) moves the extruder over the print surface according to the coordinates given by the control unit. Rheology and mix design of the printable compound are crucial to achieving a high-quality printing process.

The material must be extrudable and able to maintain its shape once deposited over the printing bed. The deposited layers should not collapse under the load of subsequent layers and a good inter-layer adhesion must be ensured for better mechanical and durability performance of the printed structure [8]. Although the benefits in reducing cycle time, labor cost, and enhancing the architectural freedom can be achieved while employing additive digital fabrication for construction, the technology remains expensive and not environmentally friendly in terms of materials. Generally, to ensure adequate extrusion flow and print quality, the use of coarse aggregates in printable mixtures is not recommended, leading to a greater consumption of cement and finest mineral fractions, which require higher energy-intensive grinding processing than large ones [8,9]. Higher utilization of energy and other natural resources in OPC and concrete production causes a severe environmental burden, involving extensive climate-altering emissions (mainly CO_2 and SO_2) and adverse pressures on soil and marine ecosystems due to the anthropogenic extraction activities [10]. Therefore, research is increasingly focused on the study and optimization of "greener" 3D-printable cementitious systems that can be integrated with the AM. Latest trends of eco-friendly materials for 3D printing concern [9,11,12].

1) The development of alternative low-carbon binders to OPC;
2) The development of printable mixtures containing under-utilised and solid wastes as aggregates.

Alkali-activated materials (AAMs) are considered most favourable candidates to replace traditional cement in E3DCP. AAMs are obtained by alkaline activation of aluminosilicate precursors, such as fly ash (FA), granulated blast furnace slag (GBFS), silica fume (SF), rice husk ash (RHA), and metakaolin (MK). Employing these industrial by-products as the major raw material for E3DCP would be desirable because it would eliminate their pullulating disposal and landfilling [13]. Furthermore, it is well recognized that the synthesis process of AAMs involves lower temperatures and energy needs than the production-cycle of OPC, bringing significantly lower carbon footprint. As supported by the life cycle assessment (LCA) study conducted by Ouellet-Plamondon and Habert [14], such characteristic is quite evident in one-part geopolymer mixtures using a single alkali activator and water like activating agent. However, a careful and well-tailored selection of the mix constituents also makes it possible to obtain "two-part" mix type with a reduced carbon footprint. A recent study conducted by the authors, investigating the environmental and technological impacts of waste material aggregates used in AAM and OPC matrices, highlighted that both the implementation of geopolymer binders and the introduction of recycled aggregates in partial substitution/total of virgin ones significantly lowered

the global warming potential over the OPC-based composites. In accordance with the LCA results, AAM-based binders reduced the carbon footprint from 30% to 45% compared to ordinary cementitious mixtures, depending on the level of substitution between virgin and recycled aggregate [15]. In addition to the environmental potential, the growing interest in AAMs derives from their engineering performances [16]: excellent mechanical strength, low permeability, high-temperature resistance, and chemical inertness. Despite these attractive characteristics, research is now addressing some shortcomings (high cost of raw materials, long-term durability behaviour, influence of curing regime on structural properties) to ensure that AAM can effectively compete against Portland cement-based construction materials [17]. Recent literature on AAMs for E3DCP demonstrated valuable results for the growing establishment of these binders in digital manufacturing. Chen et al. [18] investigated the influence of different GGBS/FA combinations on the mechanical anisotropy. Over-high-dosage of FA was discovered to aggravate the mechanical properties, interlayer pore structure, and anisotropy of printed samples due to the weak activation reactivity of FA and the higher thixotropy of FA-incorporated mixtures. Therefore, the reactivity of aluminosilicate precursors should be carefully addressed. Yuan et al. [19] conducted a multi-criteria study on extrusion-based 3D-printed alkali-activated mortars to assess the influence of mix proportion parameters (sand-to-binder ratio, FA/GGBS ratio, and silicate modulus of activator) on extrudability, buildability, and interlayer strength. According to the previous research by Chen et al. [18], the rise in the FA/GGBS mass ratio weakened the interlayer bond strength. Larger silicate modulus and sand-to-binder ratio were beneficial to the strength bond between printed filaments. However, the investigated parameters had contrasting effects on the rheology (and therefore printability) of the mixtures. Loss in extrudability and buildability were accelerated by increasing the sand-to-binder ratio, decreasing the FA/GGBS ratio, or using a lower silicate content in the activator. Sikora et al. [20] deepened the influence nano-and micro-sized additive (nanosilica, clay nanoparticles, graphene-based materials) on the printing properties of AAMs. Nanosilica and nanoclay additives can be added to improve the material's buildability as well as its early age compressive, flexural and interlayer bond strengths. Graphene-based materials were recognized as promising strategy to enhance the fresh and hardened properties of the mixtures in terms of rheology, modulus of elasticity, tensile strength, and fracture strain. Novel 3D-printed AAM foams for thermal insulation applications were produced and investigated by Alghamdi and Neithalath [21]. By implementing a surfactant foaming agent in the printable mix design without affecting the printability, the authors were able to obtain a highly porous matrix (55–75% in air void fraction) with thermal conductivities ranged between 0.15 and 0.25 W/m × K, demonstrating effective heat resistivity for wall panel applications.

The utilization of solid waste materials as aggregates to produce cementitious materials for AM can greatly promote the technology to reach its maximum cost-effective and ecological potentials. For both conventional and AM methods, the investigation of eco-friendly mixtures that replace natural aggregates with waste materials is important for addressing the shortages of natural resources and serious deterioration of the ecological environment induced by the improper treatment and low recycling rates of solid waste products [12]. Recycled fine concrete aggregates [22], waste glass [23], metallurgical by-products [24], and scrap plastics [25] are some recent examples of successful incorporation of waste aggregates into 3D-printable OPC matrices. Xiao et al. [22] found that combining recycled fine concrete aggregates and polyethylene (PE) reinforcement fibers in 3D printing mortar resulted in higher compressive, flexural, tensile splitting strengths, and deformation ability than the fiber-free mortar with virgin aggregates. Waste glass aggregates were used by Cuevas et al. [23] to design lightweight printable concrete with improved thermal insulation properties and satisfactory mechanical performance in compression and flexural. Polyethylene terephthalate (PET) aggregates were investigated by Skibicki et al. [25] to produce lightweight mix with suitable rheological properties for printing, useable in most structural elements even under varying thermal conditions (for addition of PET up to 10 v/v%).

End-of-life tires (ELTs) are considered one of the most abundant and attractive scrap products from an economic point of view. Annually, nearly one billion ELTs are generated worldwide, and this waste flow is growing dynamically. "Green" management of ELTs is an imperative for circular economy and sustainable development [26]. Rubber-concrete, where coarse and/or fine mineral aggregates are replaced by ground waste tire rubber (GWTR) from shredding of worn tires, was first introduced by Eldin and Senouci [27] in the early 90's with the purpose of finding an eco-sustainable way for the recycling end-of-life tires (ELTs), mitigating the adverse environmental and economic effects related to their accumulation in landfill, burning, or thermal processing to obtain fuel. In addition to enhancing the conservation of natural resources, the use of GWTR in place of mineral aggregates was recognized as a valuable route to confer concrete new technological peculiarities, including lightweight, less self-weight, vibro-acoustic damping, energy dissipation, toughness, ductility, impact resistance, and thermal insulation [28–30]. Although, deleterious effects on mechanical strength were verified, rubberized concrete mixtures were proposed for several non-structural applications in civil and non-civil engineering [85]: a) building members with requirements of low density, medium strength, and high toughness; b) vibrational damping in retaining structures, pavements, bridge sidewalks, industrial floors, and decks; c) thermal and acoustic insulating components; d) hydraulic structures like as dam spillways and tunnels when considerable resistance to abrasion is required; and e) in cold climatic regions where significant freeze-thaw resistance is required. In recent years, research on the possibility of incorporating GWTR into AAMs has intensified [30–32]. The "philosophy" behind this practice is always inherent to the sustainable development in construction: combining the functionality (both ecological and technological) of waste tire aggregates with the use of eco-friendlier concrete matrices, would lead to an even more significant advantage in terms of environmental impact. The additional benefit of incorporating GWTR into AAMs is the effective rubber-matrix compatibility. Comparative studies between OPC and AAM-based rubberized composites [10,32] have found agreement that the alkaline environment rich in

Table 1 – Chemical compositions (oxides) in w/w% of FA, GBFS, and SF.									
Source material	CaO	SiO$_2$	Al$_2$O$_3$	FeO	K$_2$O	Na$_2$O	MgO	SO$_3$	TiO$_2$
FA	3.47	52.18	24.16	9.55	3.75	1.47	1.29	3.21	1.14
GGBFS	45.29	33.06	10.34	–	0.71	0.31	6.61	2.39	0.67
SF	0.35	98.37	0.19	0.08	0.28	0.20	0.15	0.19	–

Sodium hydroxide (NaOH) of alkali-activated formulations as well as the presence of precursors with high pozzolanic activity (i.e., SF) improved the interfacial bonding of rubber aggregates with the matrix. Then, better mechanical, microstructural, and durability characteristics were revealed in AAMs over OPC counterparts.

Based on above literature survey and findings, the topic of replacing mineral aggregates with GWTR is not yet fully investigated in E3DCP technology. Most of the available contributions originate by the authors [8,33,34]. Results of the previous studies revealed that GWTR in place of ordinary mineral aggregates preserved suitable printability properties in terms of extrudability and buildability, enhanced the interlayer adhesion and structural compaction of the printed samples by favourably changing the surface tension and fluidity of the fresh mix, significantly reduced the mechanical anisotropy, and increased the thermo-acoustic insulation capacity of the material. Furthermore, no studies have been encountered in the literature regarding the feasibility of developing 3D-printable AAMs incorporating waste aggregates (specifically, GWTR). Therefore, the present study aims to fill this knowledge gap.

The proposed research work focuses on the development, optimization, and characterization of novel rubberized alkali-activated composites designed for extrusion-based 3D printing. By fully replacing sand with GWTR, sorted in two granulometric fractions (0–1 mm rubber powder and 1–3 mm rubber granules), the effects on extrudability and rheological properties as well as on hardened characteristics including directional compressive strength, flexural behaviour, and mechanical anisotropy degree are reported and discussed. Furthermore, the influence of rubber addition on thermo-mechanical response, damping, heat resistivity, and sound insulation of the printable composites is probed. For this purpose, dynamic mechanical thermo-analysis (DMTA), thermal conductivity (k) analysis, and acoustic insulation testing were implemented in the experimental campaign, respectively. Finally, the performances of rubberized alkali-activated composites are compared with those obtained in the OPC-based mixes investigated by the authors in previous research studies, to evaluate the effectiveness of incorporating polymer aggregates in the two printable binders.

2. Material and methods

2.1. Raw materials

A ternary blend of aluminosilicate source materials was employed to prepare AAMs. FA, supplied by Cemex (Cemex, UK), was used following BS EN 450-1 [35]. GBFS was provided by Hanson (Hanson, UK). Ultra-fine SF (grade 0.06–0.3 mm) was obtained from SIKA (SIKA, Swiss). The chemical composition of each precursor, analyzed by a Supermini 200 X-ray

fluorescence spectrometer (Rigaku, Japan), is reported in Table 1.

The mineralogical characteristics of FA, GBFS, and SF were investigated by powder X-ray diffraction (XRD), employing a D8 advanced Bruker AXS diffractometer (Bruker, Germany), with Cu-Kα radiation, wavelength of 1.542 Å, and beam radiation set to 40 kV and 40 mA. Fig. 1 shows the experimental XRD patterns processed using the software DIFFRACT.SUITE (Bruker, Germany). The diffractogram of SF show the presence of Quartzite and Calcite as major crystalline phases distributed along the entire spectrum. FA has partly amorphous behaviour between 2θ 5° and 2θ 30° along with small crystalline phases of Quartzite, Calcite, and Mullite. GBFS exhibits near-fully amorphous behaviour without any relevant crystalline phases.

Graded sand was sieved in compliance with BS EN 410-1 standard [36] to achieve two different size gradation: 0–0.5 mm and 0.5–1.0 mm. A binary solution of Sodium silicate (Na$_2$SiO$_3$) and Sodium hydroxide (NaOH) was used as an alkaline activator for making AAMs. Na$_2$SiO$_3$ solution, with the SiO$_2$/Na$_2$O mass ratio of 3.23, was supplied by Solvay (Solvay, Portugal). A 10 M NaOH solution, provided by Fisher Scientific (Fisher Scientific, Germany), was prepared by dissolving pellets with 98% purity in deionized water and cooled before use. Then, the alkali solutions, with fixed mass ratio of 2:1 (NaOH:Na$_2$SiO$_3$), were mixed at 700 rpm for 5 min, using a 230V/50Hz magnetic stirrer (Fisher Scientific, UK).

Two different size gradation of GWTR, from ambient mechanical shredding of post-consumer car tires, were kindly supplied by the European Tyre Recycling Association (ETRA, Belgium) and used "as received" in volumetric replacement of sand to produce the rubberized alkali-activated composites. These two types of rubber fractions are named *rubber powder* (RP) and *rubber granules* (RG) according to granulometry distribution. The nominal size gradations of RP ("fine" aggregate)
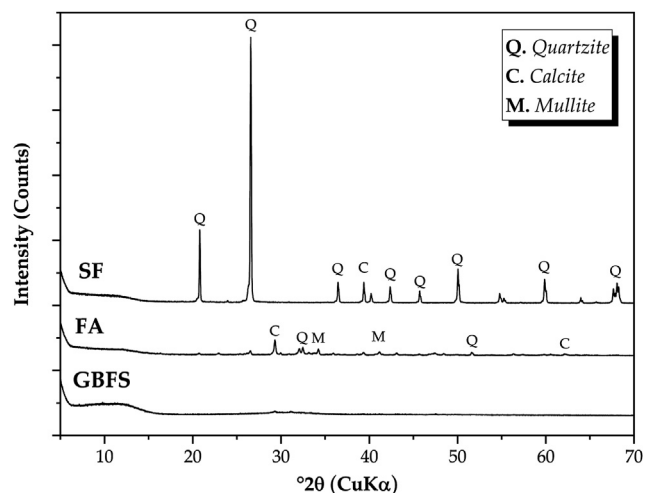
Fig. 1 – XRD patterns of FA, GBFS, and SF.

and RG ("coarse" aggregate) are 0–1 mm and 1–3 mm, respectively. The particle size distribution, conducted by standard sieving analysis [37], is presented in Table 2.

The average density of GWTR, determined by an AccuPyc 1330 He-pycnometer (Micromeritics, USA), was 1.2 g/cm³. Scanning electron microscopy (SEM) analysis, by a Mira3 FEG-SEM (Tescan, Czech Republic) was undertaken to examine the morphology of the rubber particles used in this study. The results of this investigation indicate that surface texture of GWTR varies as a function of its particle size. More irregular profile and rougher surface of RP (Fig. 2a) than RG (Fig. 2b) is due to the influence of number of grinding cycles on the microstructural characteristics. Specifically, the jagged texture in RP was caused by being shred repeatedly several times until the desired finer size gradation is met [38].

The chemical element composition of GWTR (Table 3), by using Energy-dispersive X-ray spectroscopy (Octane Elect EDS system, Edax, USA), indicated the obvious presence of Carbon (C) that derived from a) the organic nature of polymer, b) the carbon-black additive present in the tire compound, and c) the carbon-coating treatment performed before the SEM analysis to make the samples conductive. Secondary chemical elements, including Silicon (Si) and Zinc (Zn) were derived from chemical fillers typically used in the tire compounds. Particularly, Zn came from Zinc stearate, which is employed as an activator, antiadhesion agent, and lubricant in the vulcanization reaction of tire rubber. Such compound is one of the main contributors to the poor interfacial adhesion of GWTR with cement matrix. It diffuses on the particle surface, creating a hydrophobic coating that hinder the binding with the hydrophilic cement paste [10].

Attenuated Total Reflection (ATR) Fourier Transform Infrared (FT-IR) spectroscopy is used to investigate the chemical structure of ELTs-derived rubber aggregates. The spectrum was collected using a PerkinElmer Spectrum 3 FT-IR spectrometer (PerkinElmer, USA). Four scans were averaged within the wavenumber range of 4000–500 cm^{-1} considering a resolution of 4 cm^{-1}. The average FT-IR pattern (Fig. 3) showed three characteristic absorbance regions: (1) the doublet near 3000 cm^{-1} (2915 cm^{-1} and 2846 cm^{-1}) is assigned to stretching vibration of methylene groups present in polymeric chain [39]; (2) the peak at 1539 cm^{-1} and 1396 cm^{-1} correspond to the antisymmetric and symmetric stretching vibrations of the carboxyl group in Zinc stearate molecule [10], verifying the EDX analysis; and (3) the absorbance region under 1000 cm^{-1} can be ascribed to several molecular vibrations of rubber structure, including the bending vibration out-of-plane of vinylene groups (~ 1000 cm^{-1}), the stretching vibration of carbon-hydrogen (C–H) covalent bonds (~ 820 cm^{-1}), and the vibration of carbon-sulphur (C–S) bridges (~ 620 cm^{-1}) [40,41].

2.2. Mix designs

Starting from a "control" (CTR) alkali-activated formulation designed and optimized by the authors in previous studies [41,42], four rubberized composites were prepared by replacing (in volume, % v/v) the sand with RP and RG in different proportion ratios. The sample ID and aggregate proportions for each mix design are as follows: 50RP-50S (50% v/v sand - 50% v/v RP), 100RP (0% v/v sand − 100% v/v RP), 50RP-50RG (0% v/v sand − 50% v/v RP − 50% v/v RG), and 25RP-75RG (0% v/v sand − 25% v/v RP − 75% v/v RG). All mix design parameters were kept constant throughout the mix preparation except for the aggregate constituents. The mix design compositions (ratios of precursors and activators, activator-to-binder ratio, amount of water) was not altered since, as previously mentioned, the basic mix design satisfied suitable printability and strength requirements in the context of 3D concrete printing technology, including good extrudability, flow-ability, buildability and improved compaction of printed parts and mechanical isotropy. Also, the rationale behind the selection of the input materials was related to environmental reasons. Carbon-footprint analysis conducted in previous research works [10,15] verified that the proposed CTR mixture was adequately balanced to provide an environmental impact (embodied-CO$_2$) approximately 30% lower than the OPC counterpart, leading an evident benefit in terms of eco-design.

The solid ingredients (aluminosilicate precursors and aggregates) were mixed in a dry state for 5 min with a planetary mixer (Kenwood, Germany) at 250 rpm. The alkali-activator solution was then slowly added to the dry materials and the resulting mix was then stirred for 3 min at 250 rpm, followed by another 7 min at 450 rpm. The mixing continued until a homogeneous fresh compound was obtained. The mixtures were poured in the hopper of 3D printing for the printing process. For comparison purpose, alkali-activated mixes were also prepared to be cast to assess the mechanical performance of the composites as function of fabrication method. In this case, the fresh mixtures were placed in 40 × 40 × 160 mm plastic moulds. Two-step curing process was conducted. First, the moulds were treated in oven at 60 °C for 24 h. Then, after demoulding the specimens were removed from the oven and left in laboratory condition of 20 °C for 6 days. The mix design formulations are detailed in Table 4.

2.3. Extrusion-based 3D print

A gantry-type 3D printer was used in this study to test the printability of the rubberized mixtures and fabricate samples for the experimental characterization. The apparatus consisted of a metal frame and a stainless-steel hopper able to move in the X, Y, and Z spatial directions, covering a maximum print area of 1 × 1 × 1 m. An extrusion auger screw inside the hopper was connected to a motor that was then able to rotate and extrude the mix through a circular nozzle.

Table 2 – Sieve analysis results of GWTR aggregates.

RP (0–1 mm)		RG (1–3 mm)	
Sieve size	% passing by weight	ASTM sieve size	% passing by weight
1 mm	99.7	3 mm	99.13
0.71 mm	66.94	2 mm	51.28
0.425 mm	16.55	1.7 mm	22.47
0.125 mm	0.28	1 mm	1.35

(a)   (b)
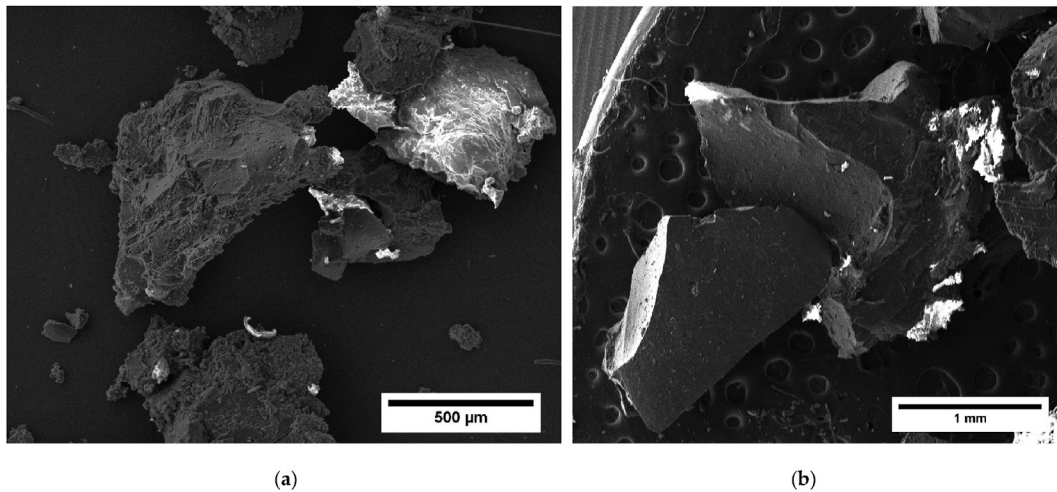
Fig. 2 – SEM microstructural analysis of (a) RP and (b) RG.

Besides, the hopper was implemented with a scraper, which aid the extrusion reliability, improving the flowability and compactness of the fresh mix and preventing nozzle clogs. A customized computer numerical control (CNC) gantry system based on the open-source extrusion rails Open-Builds platform (OOZNEST, UK) was employed as a positioning system. The motion was driven by NEMA 23 Stepper motors (Steppers, UK) equipped with TB6600 drivers. The drivers were controlled using a RAMP board which is a common 3D printers controller based on an Arduino Mega 2560 microcontroller (Arduino, UK). Klipper open-source firmware was used to control the kinematics of printing system. An in-depth technical overview of the 3D printer can be found in Ref. [41].

2.4. OPC-based 3D-printable composites for comparison

For the sake of comparison between the performance of alkali-activated and ordinary cement matrices, experimental results collected by the authors in previous research works on 3D-printable GWTR-cement composites were taken as a reference [8,33,34]. OPC-based mixes are identical to AAMs counterparts in terms of sand-GWTR replacement and RP:RG proportion ratio. Differences between the two formulations concerned the type of binder, the variability in water-to-binder ratio, and the presence of fixed content of chemical admixtures to satisfy adequate rheology and print quality. The mixtures were printed with an extrusion-based printing system, adopting the parameters presented in Table 5.

Six -layers slabs (230 × 160 × 55 mm) were produced both to inspect the printability of the compounds and to extract specimens for the hardened-state properties characterization of the materials.

2.5. Experimental program

2.5.1. Fresh properties

Before printability analysis, the flow table test method (BS EN 12350-5 [43] standard) was used to evaluate the fresh-state behavior of the alkali-activated mixes. The cone with a bottom diameter of 100 mm was placed in the center of the table, and the mix was then transferred into the mold in two parts, using the wooden tamper to consolidate each layer ten times in an even pattern. Once the sample was effectively placed in the mold, the cone was slowly removed, and the hand crank rotated 15 times over a period of 15 s. Following the 15 rotations, the diameter of the sample was recorded using a caliper after 0, 5, and 15 min. From this, the flow percentage (FP) of the mixtures was calculated using the formula (Equation (1)) below:

$$FP = \left(\frac{D_{avg} - D_0}{D_0} \right) \times 100 \tag{1}$$

where: D_{avg} - average of the two perpendicular diameters recorded for each sample after a certain time (mm), and D_0 is the bottom cone diameter (mm).

2.5.2. Printability tests and samples manufacturing

In an identical way to the printability assessment performed for the OPC-based mixes, the print quality of the AAM composites was determined in accordance with the criteria proposed by Papachristoforou et al. [44]. Extrudability was qualitatively evaluated monitoring the regular and interruptions/blockage-free extrusion and deposition of the material. Buildability was assessed by the number of layers of the printed specimen that can be achieved without collapse or significant shape deformation. At least five printed layers of cementitious material without structural failure was established as the condition to accept the mix as printable. Six-layer slabs (230 × 160 × 55 m^3) were considered "target" structures to verify the printing requirements. The nozzle diameter remarkably affects the resolution of the printed object as well as the extrudability of the cement paste during

Table 3 – EDX chemical element composition of GWTR aggregates.

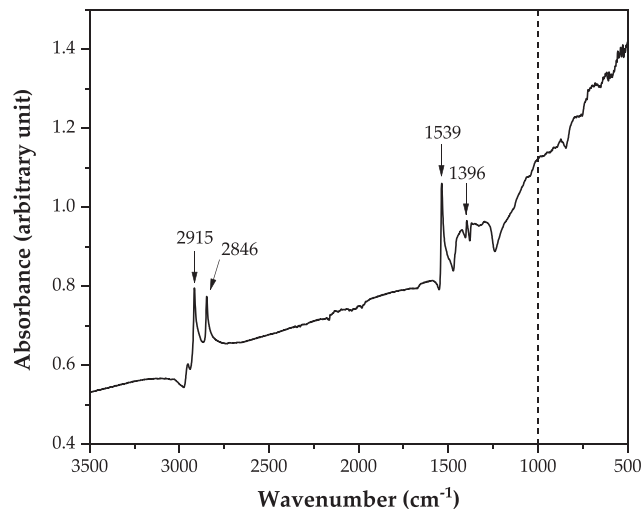| Element	Carbon (C)	Oxygen (O)	Zinc (Zn)	Silicon (Si)	Sulphur (S)
Atomic %	98.83	4.58	0.32	0.38	0.89

Fig. 3 — FT-IR spectrum of GWTR aggregates.

the process. The smaller diameter of the nozzle leads to finer details of printed structure [41]. Conversely, larger nozzles allow the ease of paste flow, minimizing undesired pressure gradients at the nozzle area and promoting a continuous and smooth extrusion process [45]. To investigate how the rheology of alkali-activated composites behaves as a function of the nozzle diameter, three different orifices were analysed: 10 mm, 15 mm, and 20 mm. Printability test were conducted at 25 mm/s printing speed, maintaining the other parameters (print path and layer height) like to those selected for OPC mixes. Once the nozzle size and mix rheology were optimized, the slabs resulting from printability tests were cured following the same procedure use for mold-cast samples (oven-treatment at 60 °C for 24 h + 6 days under ambient temperature curing). After that, specimens for materials' characterization were cut by diamond blade sawing.

2.5.3. Unit weight

Following the standard method BS 1881-114 [46], the unit weight of the samples was determined as the ratio between the oven-dry mass of specimens (110 °C for 48 h), measured by a Mettler Toledo analytical balance (Mettler Toledo Ltd., USA), and their geometric volume, by means of a digital caliper (0.05 mm sensitivity). For each formulation, four samples (40 mm × 40 mm × 160 mm beams) were measured and the average value of unit weight was reported.

2.5.4. Static mechanical testing

Static mechanical tests (Fig. 4), conformed to BS EN 196-1:2016 standard [47], were performed using a 150 kN universal testing machine (Instron 5960, United Kingdom).

3D-printed and mold-casted beams (40 × 40 × 160 mm), extracted from the slabs, were tested for their flexural strength (three-point configuration). The loading speed and span distance were 1 mm/min and 100 mm, respectively. The values of flexural strength (σ_F) are the average of values recorded from three specimens in which the loading direction was perpendicular to the printing path. Post-failure beams were processed to obtain 40-mm side cubes for compressive test (six specimens for each formulation). The test was conducted at a loading rate of 1 mm/min 3D-printed cementitious elements are prone to provide anisotropic mechanical behaviour because of the dependency of performance upon the loading direction with respect to the printing direction [48]. In this experimentation the influence of the loading direction on the mechanical behaviour was investigated. Compressive strength (σ_C) was determined by testing the printed specimen in two different orientations labeled as "Z" (compression load perpendicular to the filament plane) and "X" (compression load applied along the filament plane). For each loading orientations three cubic specimens were tested, and the average values of σ_C-Z and σ_C-X were reported. Same number of testing items was considered for mold-casted samples. Then, the degree of mechanical anisotropy was quantified using a parameter, named anisotropic degree (AD) and defined by Xiao et al. [22], which can be calculated as the percentage variations of the maximum and minimum σ_C in the two loading directions (Equation (2)):

$$AD = \frac{Maximum\ \sigma_c - Minimum\ \sigma_c}{Minimum\ \sigma_c} \times 100 \qquad (2)$$

2.5.5. Dynamic mechanical thermo-analysis (DMTA)

DMTA was performed to measure the dynamic mechanical response of alkali-activated and cementitious composites to an oscillatory strain as a function of temperature. The output results of DMTA were inspected by considering three physical properties: (1) the storage modulus (E′) corresponding to the material's elastic response and ability to store or fully recover energy, (2) the loss modulus (E″) corresponding to the material's plastic response and its ability to dissipate energy, and (3) the damping ratio (tan δ), corresponding to the ratio E''/E'. Specifically, damping is a crucial parameter of concrete

Table 4 — Mix proportions of AAM mixes.							
Sample ID	Precursor (% w/w)			Aggregate (% v/v)			Na₂SiO₃:NaOH (by mass)	a/b ratio[b]
	FA	GBFS	SF	Sand[a]	RP	RG		
CTR	60	25	15	100	0	0	2:1	0.4
50RP-50S	60	25	15	50	50	0	2:1	0.4
100RP	60	25	15	0	100	0	2:1	0.4
50RP-50RG	60	25	15	0	50	50	2:1	0.4
25RP-75RG	60	25	15	0	25	75	2:1	0.4

[a] Graded sand contains 60% w/w of 0—0.5 mm size fraction and 40% w/w of 0.5—1.0 mm size fraction.
[b] a/b ratio refers to activator-to-binder ratio.

**Table 5 – Printing process parameters adopted for OPC-based mixes.**

Nozzle diameter	Nozzle shape	Layer height	Printing speed	Print path
10 mm	Circular	10 mm	33 mm/s	Linear path

materials for vibration control, noise reduction fatigue endurance, and impact resistance in structures [49]. The aim of the study was to investigate the effect of GWTR aggregates on the dynamic and damping properties as well as the thermo-mechanical behaviour of the two matrices. A lot of studies revealed that the ceramic-like characteristic of alkali-activated binders confer them excellent heat resistance compared to OPCs [14]. Therefore, DMTA was also implemented to obtain evidence about the structural integrity and thermal stability of the investigated samples.

DMTA was conducted with a DMA 242E Artemis (Netzsch, Germany) thermal analyzer, testing beam specimens (60 × 10 × 4 mm) in three-point flexural mode (Fig. 5). Regarding the test parameters, the experimental protocol proposed by Damiani et al. [50], which similarly to the present work investigated cement pastes incorporating waste tire aggregates, was followed. Specimens were tested with a temperature sweep ranging from 30 °C to 200 °C, heating rate of 5 °C/min, constant frequency of 1 Hz, and strain amplitude of 0.01 mm.

2.5.6. Thermal conductivity (k) analysis

The thermal insulation capacity of the samples was investigated by k measurements conducted by a C-Therm TCi device (C-Therm Technologies, Canada) in accordance with ASTM D7984 [51] standard. Operating principle consisted in applying a known current to the sensor's spiral heating element, providing a constant one-dimensional heat flux to the sample. The applied current results in a rise in temperature at the interface between the sensor and the specimen, inducing a change in the voltage drop of the sensor element. The rate of increase in the sensor voltage was used to determine the thermal transport properties of the test material, as the voltage is factory-calibrated to temperature. Prior the analysis, prism
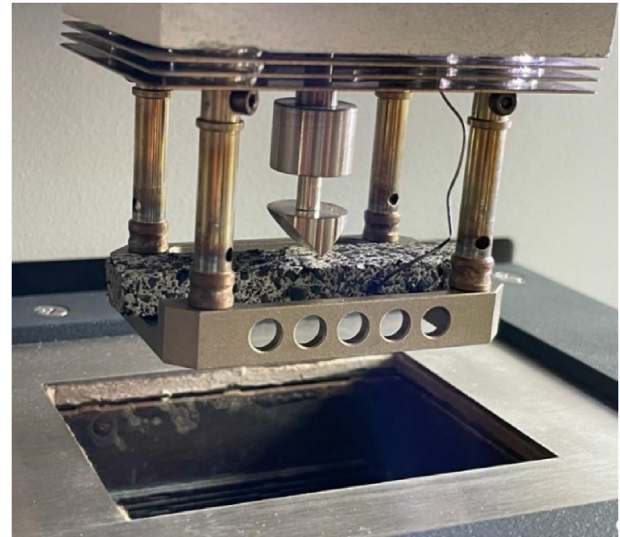
Fig. 5 – Test configuration for DMTA.

specimens (50 × 40 × 20 mm) were plane-cutted and faces were polished to ensure flatness. Then, bi distilled water was applied between the sample and the sensor to reduce the contact resistance and accomplish with testing requirements. Tests were repeated three times on each sample (four samples per formulation) and average values of k were noted.

2.5.7. Acoustic insulation analysis

Acoustic insulation properties were tested by impedance tube measurements following a test method implemented by the authors in previous works [33,52]. The acoustic experimental setup is displayed in Fig. 6. By placing the sample in the middle of the measurement system and subjecting it to an acoustic signal of specific frequency, the sound attenuation ability of the material was measured like the difference (D) between the incident sound pressure level and the transmitted sound pressure level by means two microphones positioned before and after the specimen. D-values were recorded in two frequency bands: low-medium frequency range (63 Hz, 125 Hz, 250 Hz, 500 Hz) and high frequency range (1000 Hz, 2000 Hz,

Fig. 4 – Static mechanical test configuration: flexural test (left) and compressive test (right).
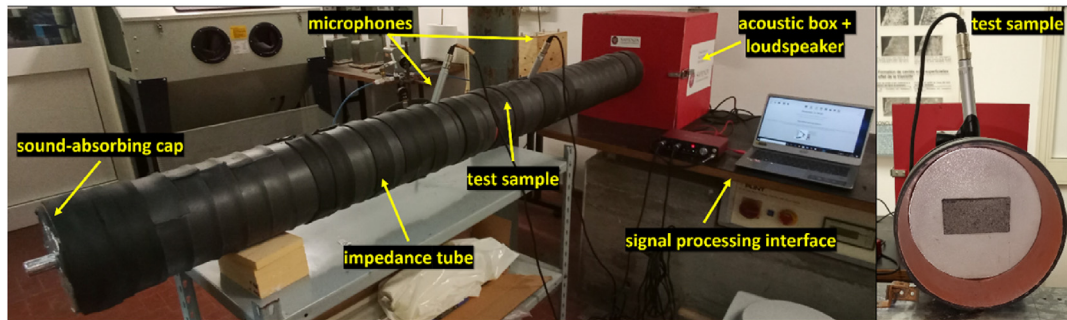
Fig. 6 – Test setup for acoustic insulation analysis.

3000 Hz, 4000Hz). Then, the sound reduction index (SRI) was computed by averaging the D-values in the two frequency bands under examination. SRI is a single number quantity (in dB) which characterize the peculiarity of materials or building elements in restricting the passage of sound through them, determining the effectiveness as noise insulators.

3. Results and discussion

3.1. Fresh properties

Fig. 7 shows the flowability of the alkali-activated mixes using the flow table test. The sand-GWTR replacement led to a significant decrease in flow properties. These results confirm the findings verified by other research works. Rubber aggregates form an interlocking structure resisting the normal flow of concrete under its own weight [27]. The reduction of the slump flow was also attributed to the clear difference in the shape and texture of rubber particles compared to the shape and texture of the replaced sand. The rubber particles are poorly shaped with rough surfaces compared to the relative smoothed surface of natural sand particles. This leads to slow relative movement of rubber particles in the matrix compared with the relative movement of sand particles, which results in an incompatible mix having reduced workability [53].
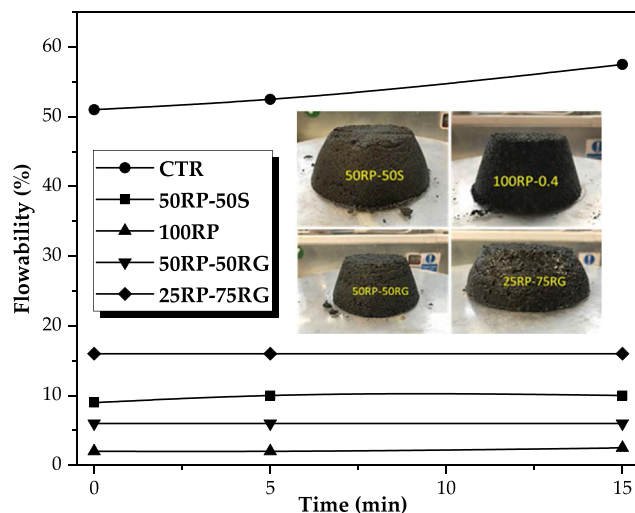

Fig. 7 – Flow table test results.

Furthermore, the increase in air content, due to the nonpolar nature of the rubber particles and their tendency to entrap air in their rough surface texture, increase the mixture viscosity and reduce the flowability [54]. Among the rubberized mixes, the lowest and highest flowability was achieved by 100RP and 25RP-75RG with an initial flowability values of 2% and 16%, respectively. This result revealed that the presence of coarse polymer aggregates (RG) would lead to a gain in flowability. The surface of rubber particles held air which entered the fresh paste. Fine rubber (RP) has higher specific surface; therefore, finer GWTR tends to entrap more air than the large-sized polymer particles. Lower rate of incorporated air means a less stiff and more fluid mixture [55].

3.2. Printability tests

Rheological measurements enabled the mix design optimization in accordance with the printability requirements considered in the experimental program and the printing system used in this work. 25RP-75RG sample was the only mixture that met the printability requirements suitable for the process. Regarding the other rubberized formulations, it was necessary to add extra water to obtain an extrudable mix. In addition, attempts were made to print using different nozzle diameters (10 mm, 15 mm, and 20 mm). Diameters of 10 mm and 15 mm were not suitable for printing. Indeed, preliminary tests revealed that using small sized nozzle required very high shear force to extrude the material due to the great viscosity of alkali-activated mix. This condition led to mix phase segregation during printing and a poor material's extrudability (Fig. 8a). Furthermore, as verified by flowability tests, GWTR addition increased the setting time of the fresh mixture. Using the smallest nozzle, this setting phenomenon occurred, blocking the material's deposition (Fig. 8b).

The influence of GWTR incorporation on the rheological properties of the alkali-activated binder is quite different than that revealed by the authors in the 3D-printable Portland mixes, where an improved fluidity was detected following the addition of the polymer aggregate [33,56]. In this case, when sand was replaced by GWTR, the local free water around the rubber particles was increased due to their lower water absorption and hydrophobicity, making the printable mix adequately fluid for printing. Conversely, the action of NaOH-based activator in the alkali-activated formulations would enhance the affinity of rubber aggregates with the binder promoting the hydration of the matrix around the rubber
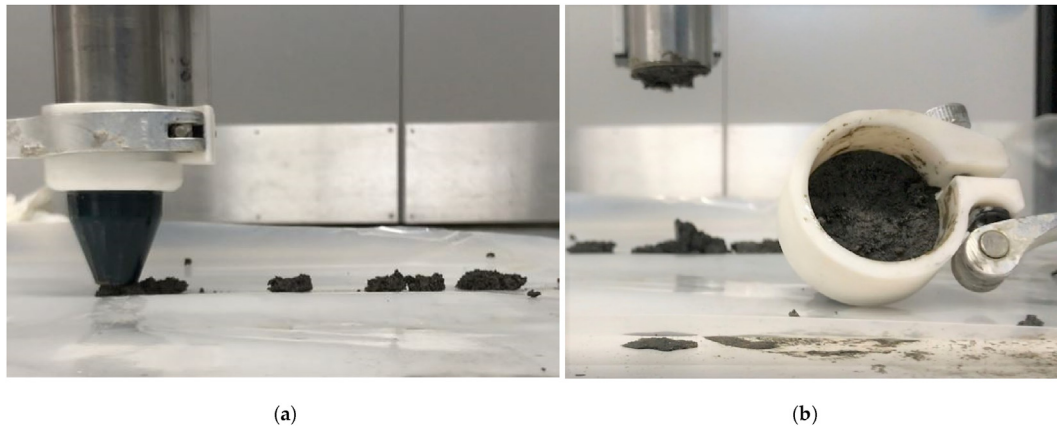
Fig. 8 – Printing issues during preliminary printing test using 10-mm diameter nozzle: (a) poor extrudability and (b) nozzle blockage.

particles and making them less able to ensure an adequate amount of free water in the mix. This effect was demonstrated by Youssf et al. [57], who observed worsening in workability of rubber-concrete mix after pre-treatment of crumb rubber aggregates in alkali solution. Moreover, it is worth noting that the different rheological behavior of rubberized Portland and alkali-activated composites is also to be attributed to the different amount of water used in their production. The rheological behavior of AAMs is assisted by the water produced in the polycondensation process of the aluminosilicate network. Then the liquid amount used is decidedly lower than OPC-based mixes, leading to increased viscosity and consequently decreased workability of the fresh mixture.

Six-layer rectangular slabs, for each AAM formulations, were successfully printed with 20 mm-diameter circular nozzle. An overview of the printing process is illustrated in Fig. 9.

3.3. Unit weight

By using lightweight rubber aggregates in place of mineral ones caused a unit weight reduction both in alkali-activated and Portland-based samples (Fig. 10). All the rubberized mixtures designed and investigated in this work provided unit weight values of less than 1800 kg/m^3 satisfying the classification as "lightweight concretes". For their low density, good thermal and acoustic insulation, and reduced self-weight, lightweight concretes have become a focus of interest in a wide range of building applications due to their engineering versatility [58].

The comparison between casted and printed AAM specimens highlighted no remarkable difference in terms of density. The unit weight of 3D-printed CTR and 25RP-75RG samples (2286 kg/m^3 and 1601 kg/m^3, respectively) was prone to increase slightly compared with mold-casted counterpart (2148 kg/m3 and 1568 kg/m^3). This was because the printing methodology could induce densification and compaction of the material due to the application of high pressure during the extrusion [42]. It should be noted that this effect occurred in the alkali-activated formulations where no additional water

was added to adjust the rheology for printing. The 3D-printed rubberized composites incorporating additional water showed lower densities than the casted samples. In this case, the extra-water added to achieve adequate fluidity for extrusion would have no role in the alkali-activation reaction. Evaporating during the curing phase, the excess water would release voids inside the material thus affecting its unit weight. This evidence is well supported by Aliabdo et al. [59], who also verified that excess water would tend to dilute the alkali activator and thus slowed down the dissolution and reaction of the aluminosilicate precursors, hindering the proper microstructural and strength development of the binder.

The comparison between 3D-printed AAM and OPC mixes can be comprehensively interpreted considering the unit weight reduction rate for the same type of sand-GWTR replacement. With respect CTR-OPC mix (1927 kg/m^3), density drops of 14.8%, 30.5%, 15.7%, and 23.8% were detected in 50RP-50S, 100RP, 50RP-50RG, and 25RP-75RG samples, respectively. Although the alkali-activated CTR mix was denser than the OPC counterpart, the incorporation of waste rubber resulted in stronger density reduction rates: −23.9% in 50RP-50S, −41.7% in 100RP, −35.5% in 50RP-50RG, and −29.9% in 25RP-75RG. This evidence was already explored by the authors in a previous research work [10], attributing the higher density decrement in rubberized alkali-activated composites to the contribution of GWTR in altering the chemistry (in terms of Si/Al ratio) and microstructural characteristics of the material.

3.4. Static mechanical testing

3.4.1. Three-point flexural test
The flexural performances of 3D-printed and mold-casted alkali-activated composites are shown in Fig. 11, where σ_F results of OPC-based mixes are also provided as a comparison.

Regardless of the type of binder (AAM and OPC) and manufacturing process (3D printing and mold-casting), the replacement of the mineral aggregate with GWTR results in a deterioration of the strength properties, depending on sand-rubber replacement level and size gradation of the polymer

Fig. 9 — 3D printing of rubberized alkali-activated composites (100RP mix is reported in the photographs).

aggregates embedded in the matrix. Primary causes for the decrease in the overall mechanical strength of rubberized materials are the hydrophobic nature of rubber causing weak and porous interfacial transition zones and its lower elastic modulus inducing high stress concentration and crack propagation inside the surrounding matrix [8,10,30,31]. It is evident that rubberized cementitious materials are not intended for load-bearing applications. The interest is directed towards their use in lightweight and resilient structures with improved thermo-acoustic efficiency. In this regard, following the ASTM C330 standard [60], the minimum strength requirement for structural lightweight concrete class is 2 MPa. As can be seen from the plot in Fig. 11, all AAM-based samples (both mold-casted and 3D-printed) met or are very close to this performance indicator. With regard the OPC-based samples mixes, the recommended requirement was just fully satisfied by 50RP-50S and 50RP-50RG mixes. Therefore, a careful optimization of the mix design and process should be address for the purposes of scaling the material for practical applications.

The comparison between printed and casted AAM-based specimens revealed no significant differences, indicating that the rheology of the mixtures as well as the process parameters were properly optimized for printing. Then, flexural behavior would results scarcely affected by the structural defects typically induced by additive fabrication (inter-filament voids or poor layer-by-layer adhesion). The discrepancy rate between σ_F-values of casted and 3D printed alkali-

activated samples varied from 0.8% in CTR mix (σ_F-casted = 8.92 MPa, σ_F-printed = 8.98 MPa) to 67.6% in 25RP-75RG (σ_F-casted = 1.76 MPa, σ_F-printed = 2.95 MPa). Such range was sharply lower than common results found in the relevant literature on E3DCP technology. Indeed, by reviewing experimental data from inherent research papers, Hou et al. [61] found that the difference in flexural strength between casted and printed samples involved ranges from 54.5% to 157.1%. Among the fully rubberized AAM formulations, highest strength performance was detected for 25RP-75RG mix. In line with the unit weight results discussed above, not adding extra-water to the fresh mix would mitigate the development of porosity in the material, ensuring better microstructural and strength characteristics.

3D-printable alkali-activated composites performed better in terms of mechanical resistance with respect to OPC-based samples. As already demonstrated by the authors in a previous work comparing mold-cast rubberized OPC and AAM composites [10], the higher interfacial affinity experienced by rubber aggregates with the alkali-activated binder is the main reason for the improved mechanical behavior under bending. By correlating the mechanical performance with the size gradation of GWTR aggregate, it can be seen how the addition of coarse RG had an improved effect on the flexural behavior compared to sample incorporating only fine rubber (100RP). The elongated and fiber-like shape of RG particles would induce better capacity to arrest local cracks and hinder
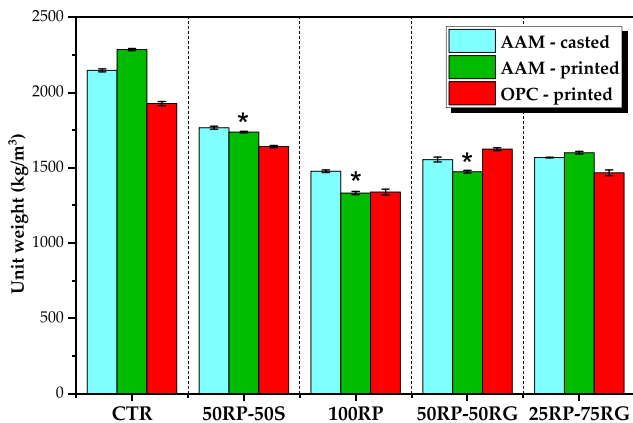

Fig. 10 — Unit weight test results. (Note that * indicates formulations where extra-water was added).
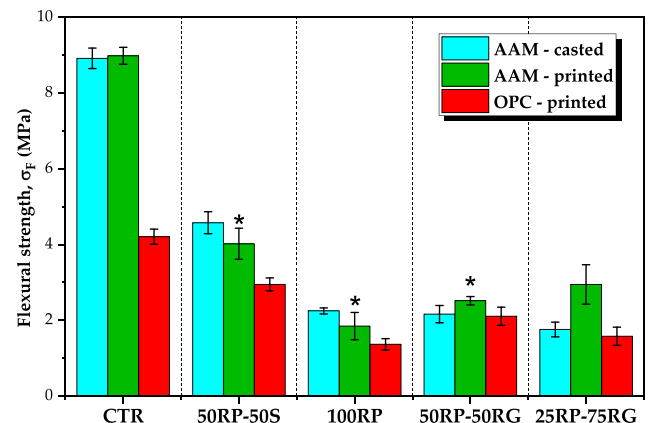

Fig. 11 — Flexural strength (σ_F) test results. (Note that * indicates formulations where extra-water was added).
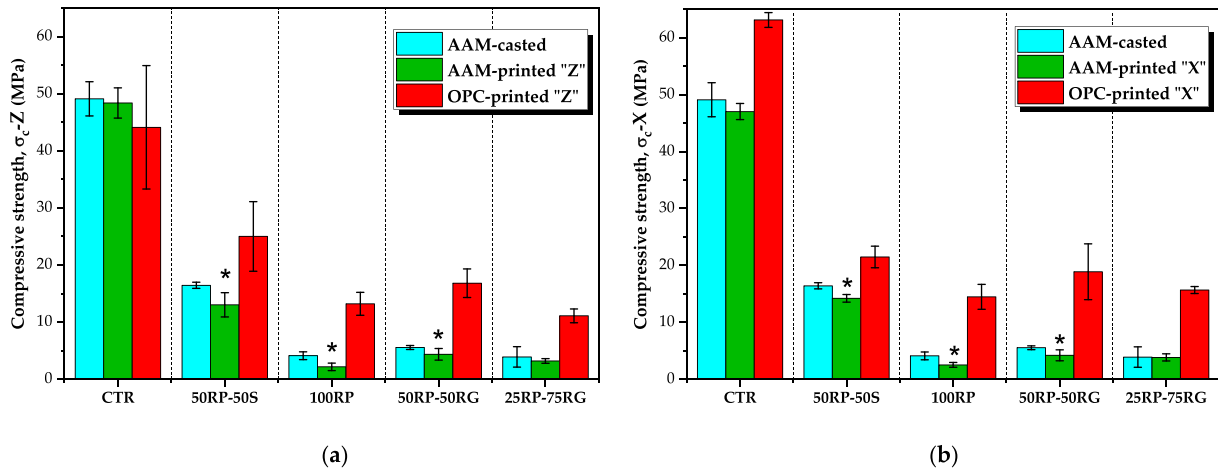
Fig. 12 – Compressive strength (σ_C) test results: (a) Z-loading and (b) X-loading. Note that "*" indicates formulations where extra-water was added.

fracture propagation effectively before the crack passes through them. Although, the finer fraction exhibits greater specific surface area than the coarse rubber, and ideally it should ensure more contact surfaces with the surrounding matrix and therefore greater interfacial bonding, the crack arresting effect would be less efficient due to its particle-shaped characteristics (low aspect ratio). This finding was argued by Liu et al. [62] investigating the influence of glass particles gradation on flexural strength of 3D-printed concrete samples loaded perpendicularly to the printing direction ("Z"). Considering the mixtures with 100 v/v% of GWTR, highest σ_F-values were detected in 25RP-75RG sample for AAM binder (2.95 MPa) and 50RP-50RG for OPC binder (2.11 MPa). This would mean that due to the improved compatibility of rubber with the alkali-activated matrix, high content of RG is admissible in AAM-based. Conversely, by analyzing the OPC-based samples, the RG concentration should be carefully dosed. There is a decrease in σ_F for the mix with higher dosage of RG (25RP-75RG), which is attributable to the interfacial defects triggered by coarse rubber aggregates that would predominate over their mechanical functionality.

3.4.2. Compressive test

In line with flexural test results, an expected loss in σ_C using GWTR instead of mineral aggregates can be observed (Fig. 12). The mean results of σ_C revealed that among the rubberized composites only two OPC-based formulations, specifically 50RP-50S and 50RP-50RG, satisfied the strength requirement of 17 MPa recommended by ASTM C330 standard [60] for structural lightweight concrete class.

Then, following the addition of GWTR, the compressive behaviour would seem to undergo a more detrimental degradation than flexural strength GWTR would perform its maximum function of inducing tough behaviour in concrete under bending load. Indeed, the behaviour of rubberized materials is governed by the crack-bridging force provided by the rubber inclusions (especially large-sized aggregates), which is related to their bending strain capacity across cracks [63]. On the other hand, the mechanical characteristics in compression are less efficient. In this case, the strength closely depends on the microstructural quality and load-bearing capacity of the matrix. Specifically, because of the weak interfacial bonding with the matrix, rubber aggregates are prone to failure at lower applied loads. Overall, alkali-activated composites exhibit lower compressive performance than OPC counterparts. This evidence confirms the results of a previous work [10], where it was shown that the presence of GWTR in place of sand, in addition to mechanically deteriorating the material by acting as a weaker aggregate, shifts the Si/Al elemental ratio out of the optimal range hindering the proper strength and microstructural development of the matrix. This finding was identified by the authors as a crucial point on which to address future research, which is to tailor the AAM mix designs over rubber aggregates while improving the strength characteristics of the matrix and preserving suitable printing properties.

Mechanical anisotropy was recognized as one of the most concerning issues for E3DCP. Because of the inherent nature of the extrusion-based deposition process, printed structures tend to be influenced by the dependence of mechanical strength on the printing direction. The rheology of the printable mixture as well as the quality of the additive manufacturing process are crucial to ensure optimal compaction between the deposited filaments, avoiding the formation of weak interlayers that can be impeding in terms of structural and durability properties [18]. The influence of GWTR aggregates on the print quality of the two binders can be assess by AD results displayed in Fig. 13. Based on the results from previous works [8,33], replacing the sand with rubber induced a reduction in the mechanical anisotropy, resulting from an improvement effect on the fresh mixtures fluidity and therefore inter-filament adhesion. Opposite trend occurred for AAM-based composites. In this case, slight increase in AD-values can be detected, justifying the different effect that GWTR induced on the rheological properties of the two matrices. However, comparing the two binders, the structural print quality of the alkali-activated formulations was better than that of the OPC formulations. All AAM mixes
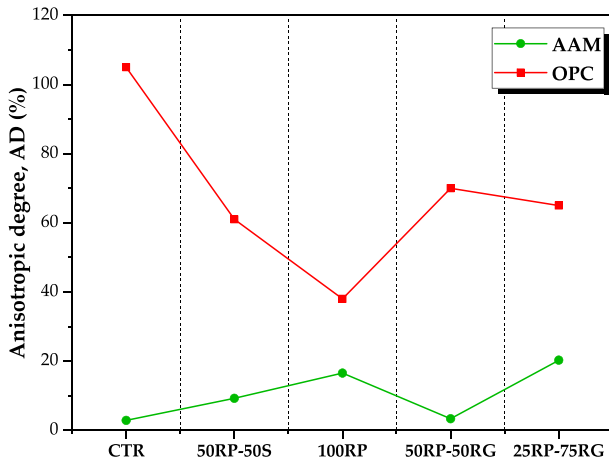
Fig. 13 − Anisotropic degree (AD) analysis of 3D-printed AAM and OPC-based composites.

3.5. Dynamic mechanical thermo-analysis (DMTA)

With DMTA, for each binder, the following samples were investigated: CTR, 100RP, and 25RP-75RG, to evaluate both the dynamic thermo-mechanical behaviour of the two matrices with and without the addition of the rubber aggregates and the influence of the particle size gradation on the damping properties. Fig. 14a compared E′ as a function of temperature of alkali-activated and ordinary cement CTR samples (0 v/v % of GWTR). AAM binder was shown to be more thermo-mechanically performing and stable over OPC sample in the covered thermal range. For both matrices, with increasing temperatures there was a decrease in the dynamic modulus of the samples but following to markedly different trends. OPC sample showed a severe drop in dynamic stiffness around 120 °C. Within this thermal region, several heat-induced microstructural degradation events occur in OPC, including damage from loss of chemically bonded water (~ 120 °C), decomposition of gypsum and ettringite (110−170 °C), and dehydration of calcium silicate hydrate (C−S−H) gel (~ 180 °C) [65]. Better dynamic mechanical behaviour was detected in CTR-AAM sample. Excellent thermal resistance was demonstrated by alkali-activated binders due to the stable network structure of abundant oxides and the presence of mineral phases that are hard to decompose at elevated temperatures. Except for the shrinkage due to the free water evaporation, the first significant degradation mechanisms occur at temperatures between 400 and 600 °C corresponding to the dehydration of calcium aluminate silicate hydrate (C-A-S-H) gel, the main binding phase in AAM [66]. Besides, the ceramic-like nature of the alkali-activated matrix would induce sintering and densification as the temperature rises, with consequent improvement in terms of thermo-mechanical response [67]. From Fig. 14b, a systematic reduction in E′ was observed in the rubberized composites mainly resulting from the lower modulus of elasticity of rubber aggregates than sand. The thermo-mechanical stability of the alkali-activated matrix promoted greater dynamic stiffness of the AAM-based composites compared to the OPC-based ones. By investigating the
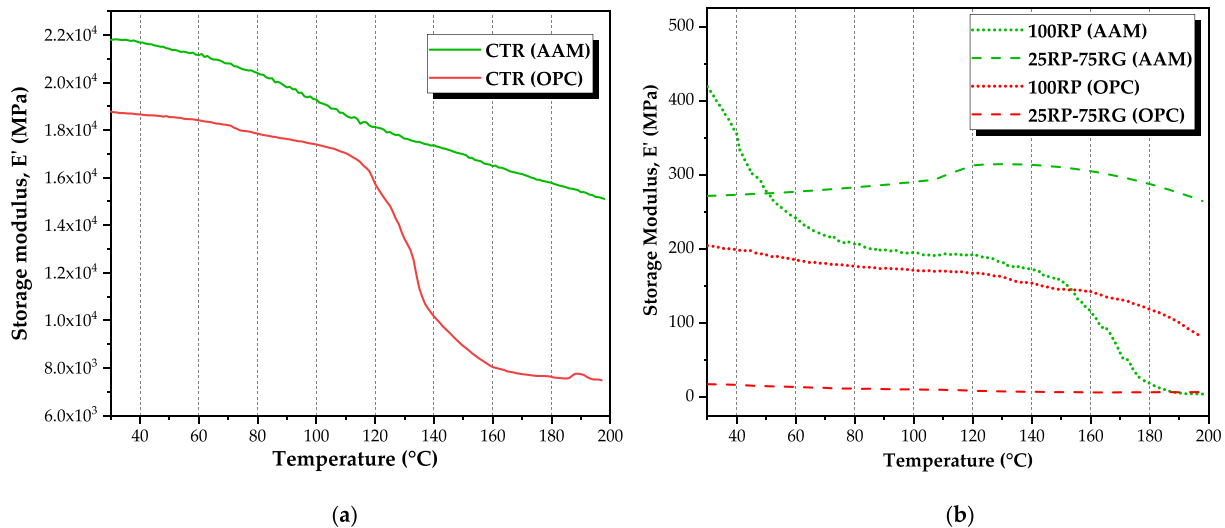
exhibited markedly lower AD-values than OPC-based counterparts, demonstrating the setting of a well-designed AM process to integrate GWTR into printable alkali-activated materials. Regarding this result, the use of nozzles with different dimensions for the extrusion of the AAM (20 mm diameter) and OPC mixtures (10 mm diameter) must be considered. A larger-sized nozzle implemented for the alkali-activated composites resulted in wider printed filaments and greater contact surface between the deposited layers, minimizing the effect of the interlayer interfaces on the strength performance [64]. The literature survey conducted by Hou et al. [61] highlighted that the mechanical anisotropy in compression for the E3DCP technology typically ranged from 67% to 115%. The results for OPC mixes are consistent with this interval (from 105% for CTR sample to 38% for 100RP sample). For AAM samples, significantly lower values were found (from 20% for 25RP-75RG sample to 3% for CTR sample), verifying the higher print quality achieved while incorporating waste aggregates in the mixes.

(a)

(b)

Fig. 14 − Storage modulus (E′) test results: comparison between (a) CTR samples and (b) rubberized composites.
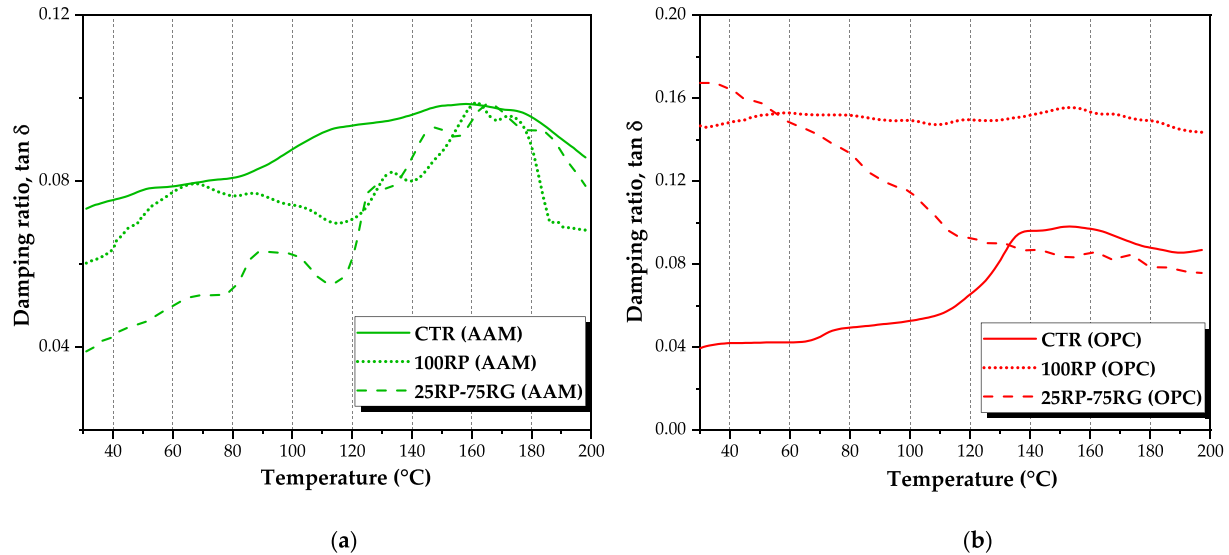
Fig. 15 − Damping ratio (tan δ) test results: (a) AAM samples and (b) OPC samples.

influence of GWTR size in AAM samples, it was noted that the presence of RG (25RP-75RG sample) induced superior mechanical stiffness for most of the investigated thermal range compared to the sample with only fine rubber (100RP sample). The difference in unit weight is the primary reason for the divergence in the dynamic behaviour of the two formulations. In Fig. 10, it was verified that the decrease in density was more prominent in 100RP mix, that is when the average aggregate size is lower. At the same sand-GWTR replacement level, the overall amount of rubber in 100RP mix was higher than that in 25RP-75RG because of the greater packing density of the fine GWTR. Therefore, in line with the decline in mechanical strength, a higher concentration of rubber per unit of volume embedded in the material would induce a more noticeable decrease in dynamic stiffness. Further aspect that can be considered in explaining the different thermo-mechanical behaviour of the two samples was the addition of extra-water considered in the 100RP mix to achieve rheology suitable for printing. Fig. 14b showed that between 40 and 80 °C, 100RP sample experienced a clear decrease in E′ presumably due to the structural losses induced by the evaporation of the excessive water. In line with this, Sayahi et al. [68] found a clear relationship between water-cement (w/c) ratio and plastic shrinkage phenomena in concrete systems: high dosage in mixing water would increase the cracking risk due to the rapid and excessive evaporation of the unbonded water which is not involved in the material's hydration. According to Gupta et al. [69], increasing water content would promote the formation of a more porous microstructure worsening the static and dynamic performance of the composite. Based on authors' previous works [8,10,33], while the rough and jagged micromorphology of RP particles assisted their mechanical gripping with the OPC paste, RG aggregates was more prone to develop interface defects due to their lower specific surface area. Hence an inadequate load transfer between rubber particles and matrix, induced by the widespread presence of ITZ defects could be the main cause of the poor dynamic modulus performance found in 25RP-75RG sample.

The results of tan δ in Fig. 15 provide a comprehensive view on the dampening properties of the investigated composites. The use of waste tire rubber to improve the damping performance of cementitious matrices was extensively explored by researchers [69−71]. Thanks to the energy dissipative characteristics of rubber related to its viscoelastic nature, rubberized cement-matrix materials highlight a marked improvement in damping ability over ordinary concretes. A summary of studies presented in Chi et al.'s review [71] revealed that by adding GWTR as part of the aggregate into unreinforced concrete allowed an increase in damping capacity up to 430% depending on rubber particle size and substitution level with the mineral fraction. In this work, the damping properties appeared to be strongly affected by the type of binder. Complementarily to E′ results, the lower dynamic stiffness detected in OPC-based samples than AAM ones implied superior damping capacity. As determined by Najim and Hall [72] the damping capacity strictly refers to the material's strength: damping is greater for low-strength concrete materials than high strength such that damping has a positive correlation with the material's ductility rather than its stiffness. Considering the bending load experimental configuration of DMTA, this finding agrees with the best flexural strength properties of AAM composites over OPC-based samples discussed in Section 3.4.1. It is worth noting that the alkali-activated composites engineered with GWTR did not lead to any improvement in tan δ with respect to CTR sample (Fig. 15a). On the other hand, the influence of rubber aggregates in OPC matrix was to significantly improve the damping capacity of composites (Fig. 15b). Major remark regarding the discrepancy in damping capacity is the different interfacial adhesion experienced by rubber into the two binders. A prior microstructural analysis reported in Ref. [10] revealed that there is a stronger bond interaction between rubber and the alkali-activated matrix than that investigated in OPC composites. Poor interfacial bonding found in OPC samples, while unsatisfactory for the mechanical stiffness and strength, could result in very high mechanical damping

[72]. A weak inter-locking between rubber and the cement matrix would make easier activating interfacial slip under the cyclic load. Assisting the vibration of the polymeric particles would therefore trigger energy dissipative mechanisms both related to the aggregates' viscoelasticity and to the frictional sliding at the GWTR-matrix interface [71,73]. In good agreement with literature [71], finer rubber (RP) provided a greater incidence on increased damping than coarser polymeric fraction (RG) in both binders.

3.6. Thermal conductivity (k) analysis

The thermal insulating properties of AAM and OPC composites were evaluated in terms of k (Fig. 16). First, the analysis revealed clear difference in heat conductivity between the CTR samples: alkali-activated concrete showed higher k-value than plain Portland mix. Wongsa et al. [74] claimed that the thermal properties depend on types of source materials, including aggregates and precursors, and density/porosity of hardened concrete. The primary factor affecting thermal performance is the intrinsic heat conductivity of the binders. The effective k-value of C–S–H gel, the dominant phase in hydrate cement system, was estimated to be 0.98 W/m × K [75]. On the other hand, the k-value for aluminosilicate gel range from 1.0 to 1.2 W/m × K, depending on Si/Al ratio [76]. Furthermore, the presence of high quantity of metal cation species in alkali-activated network (such as Al, Na, K) and the higher unit weight detected by the experimentation would explain the greater k in CTR-AAM sample than OPC counterpart.

The addition of GWTR in place of sand enhanced the thermo-insulating capacity as a function of scrap rubber content. The k of virgin mineral aggregates is around 3.5 W/m × K. Replacing the content of these aggregates with recycled rubber with lower k (∼ 0.1 W/m × K) yields a predictable reduction in heat conductivity of the composites [77]. Although the AAM matrix is characterized by higher thermal resistivity than OPC one, incorporating GWTR involved much more marked drops in k-value, at the same sand-GWTR replacement level. In OPC-based composites, with respect CTR sample (k = 1.32 W/m × K), k-value was reduced by 41%, 67%, 36%, and 39% in 50RP-50S, 100RP, 50RP-50RG, and 25RP-75RG mixes, respectively. The reduction rates for AAM-based

composites were 54%, 81%, 79%, and 74% in 50RP-50S, 100RP, 50RP-50RG, and 25RP-75RG mixes respectively, considering the k-value of CTR mix is 2.23 W/m × K.

A possible hypothesis that would explain this trend is the active influence that rubber aggregates established during the synthesis and microstructural development of alkali-activated composites. As clearly investigated in Ref. [10], rubber aggregates indirectly consume part of the NaOH activator undergoing chemical surface modification. Although, this assists the GWTR-matrix compatibility by reducing the surface hydrophobicity of the polymer particles, incomplete activation and dissolution of the aluminosilicate precursors (especially FA) occurs due to alkaline activator deficiency. In addition to revealing the intimate interfacial adhesion between GWTR and alkali-activated matrix, SEM inspection (Fig. 17) elucidates the presence of some unreacted FA, in the form of hollow glassy microspheres (cenospheres) that remained embedded in the binder acting as highly insulating fillers by virtue of their very low thermal conductivity (k = 0.08–0.1 W/m × K) [78].

According to the technical indications given by Newman and Choo [79], rubberized composites (both AAM and OPC) can be classified as lightweight insulating cement-based materials (oven-dry density range of approximately 300 to a maximum of 2000 kg/m³ and k-value of 0.2–1.0 W/m × K), aligning with the requirements of current European regulation on thermal protection, indoor comfort, and energy consumption in building [80]. Specifically, the fully rubberized alkali-activated composites (100RP, 50RP-50RG, and 25RP-75RG) widely fall within the range of foamed concretes (0.25–0.75 W/m × K), which represents the "core" technology for thermal insulating applications in construction [81].

3.7. Acoustic insulation analysis

The use of recycled tire rubber aggregates is one of the most investigated strategies to engineer, in a more eco-sustainable way, concrete in terms of acoustic insulation and noise abatement, which nowadays represent fundamental credentials in civil, urban, and residential planning [82,83]. The dissipative capacity of rubber against vibro-acoustic events allow to achieve better noise insulation performance in the cementitious media.

The acoustic insulating characteristics of AAM and OPC composites, quantified through SRI analysis (Fig. 18), showing different trends depending on the frequency range investigated. Unlike OPC-based formulations, the modification of the alkali-activated matrix with GWTR resulted in a strong improvement of the insulation properties at low-medium frequencies (Fig. 18a). With respect to CTR-AAM mix (SRI = 2.73 dB), a maximum increment of about 4 dB (+150%) was found in 50RP-50RG-AAM sample. In OPC-based samples, rubber aggregates in place of sand induced a less noticeable increase in SRI. From CTR-OPC mix (SRI = 6.51 dB) a maximum SRI-increase of about 10% was detected in 50RP-50RG-OPC sample. From these results it is evident GWTR confers acoustic improvements in the low-medium frequency range, resulting from an additional vibro-acoustic damping mechanism that rubber aggregates add to the two binders. To corroborate this assumption, an investigation conducted by
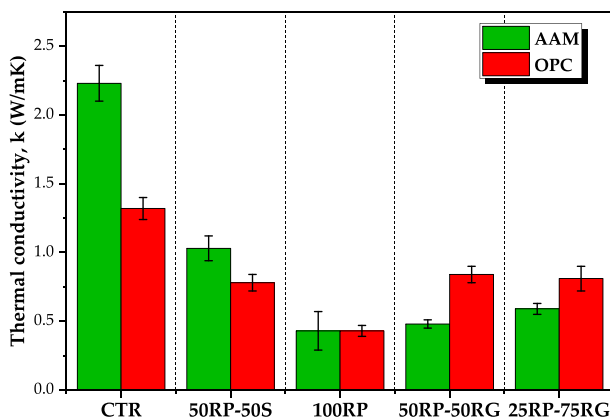
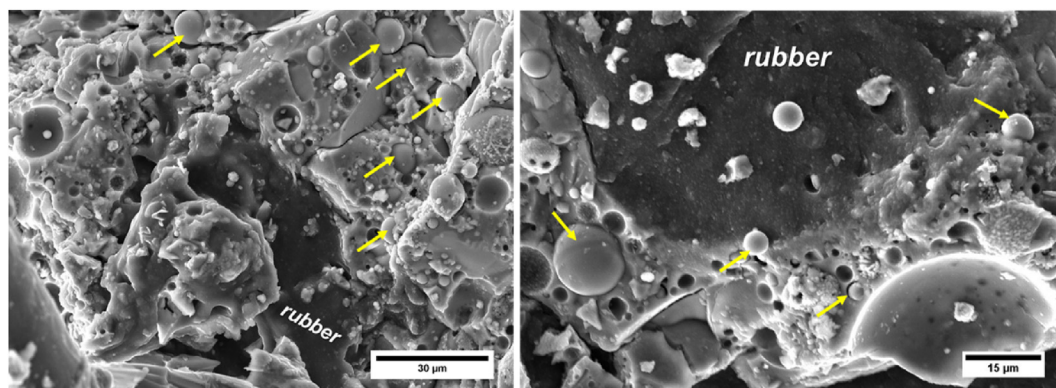**Fig. 16 – Thermal conductivity (k) test results.**

Fig. 17 — Interfacial analysis and un-reacted FA detection (yellow arrows) in rubberized alkali-activated composites by SEM.

Kumar and Lee [84] on various traditional materials used for noise reduction purposes clearly highlighted that rubber performs its maximum sound attenuating function in the acoustic range between 250 Hz and 750 Hz, which agrees with the low-medium frequency band examined in this work. As demonstrated in previous works, the presence of large-sizes rubber particles (RG) enhanced the acoustic insulation performance because of the greater impediment to sound wave propagation provided by coarse polymer aggregate over fine rubber fraction [33,85]. Hence, the use of rubber in both OPC and alkali-activated materials would provide an attractive solution for the attenuation of low-frequency noise, which is widely recognized as hard to mitigate by traditional walls and other structures causing significant physiological annoyance and distress [86].

Overall, OPC-based composites performed better in the low-medium frequency range, while AAM mixes were more acoustically effective at high frequencies (Fig. 18b). The current literature lacks similar comparative studies from which extrapolating information to explain this trend. The only relevant contribution was provided by Gandoman and Kokabi [87], which studied the sound barrier properties of waste rubber-based geopolymer concrete in comparison with the performance of ordinary concrete. They found that rubberized geopolymer composites exhibited better sound insulating behavior compared to Portland mix due to nano-porosity found in geopolymer's microstructure. Because of their nanoscale pores, through which the sound waves cannot pass, the sound barrier property was increased. However, the authors referred to an average value over a wide frequency band (100—6300 Hz) without discriminating the acoustic behavior at specific acoustic ranges. Two possible interpretations can be provided to explain the divergence of insulating performances between OPC and AAM composites as a function of frequency range.

1) Poor interfacial bonding between rubber and OPC matrix could facilitate the vibratory modes of the polymer inclusions promoting the dissipating mechanisms and noise damping characteristics of the concrete at low-medium frequencies where the contribution of GWTR seems to govern the acoustic behavior. Similar remark was reported by Zhang and Poon [88]. However, the low-frequency acoustic insulation analysis of the examined samples will require further investigations and precautions. Indeed, the impedance tube method can lose accuracy especially at low frequencies since the lower cut-off frequency of the measurement system is governed by the tube diameter.
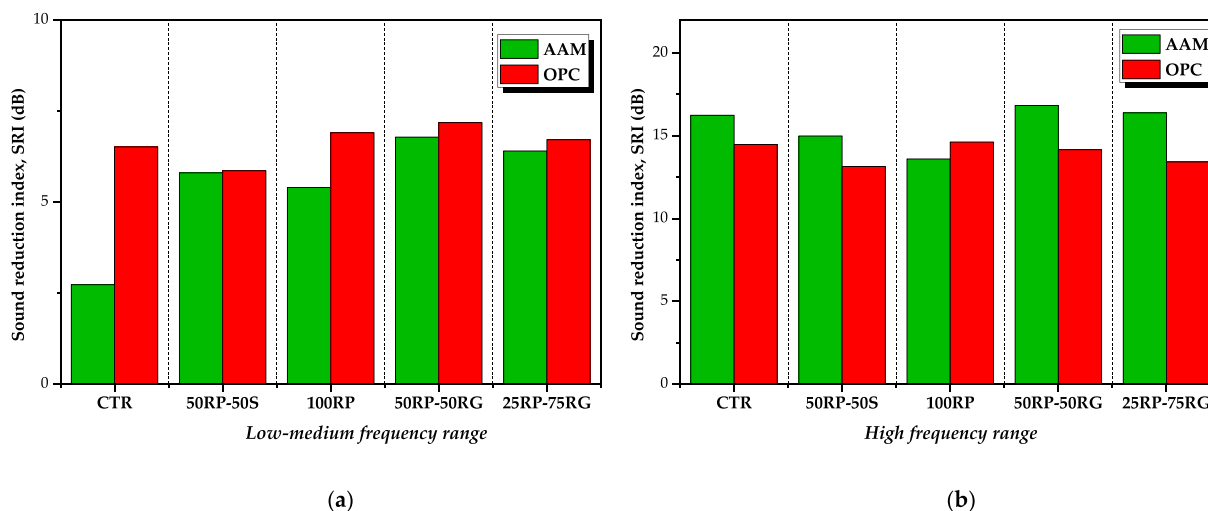

(a)

(b)

Fig. 18 — Sound reduction index (SRI) test results: (a) low-medium frequency range and (b) high frequency range.

The acoustic duct developed for the present research was designed with a diameter of 160 mm to accommodate samples with representative dimensions. In these operating conditions, the cut-off frequency is 150 Hz. Therefore, for the 63 and 125 Hz frequency bands, reverberation/reflection phenomena could occur in the tube which would negatively alter the quality of the experimental results. The verification of the results using more robust measurement systems (e.g., acoustic chambers) is proposed as the next step of the research.

2) Unit weight is one of the main characteristics determining the ability of an acoustic material to resist the transmission of sound. The primary physical property controlling the sound insulation is the mass per unit area of the element, in agreement with the well-know "mass law". At high frequency (generally >500 Hz), the insulation efficiency depends on the mass law: the denser the material, the better it insulates [89]. Comparing the two binders, except for 50RP-50RG mix, there is a good correlation in accordance with the "mass law" between unit weights (see Fig. 10) and high-frequency SRI values. In the high-frequency acoustic spectrum the dissipative functionality of rubber aggregates competes with the attenuation mechanisms dictated by the "mass law", therefore the effect of GWTR addition on the acoustic insulation improvement is less evident.

4. Conclusions

This research aimed to design and investigated novel 3D-printable alkali-activated composites engineered with GWTR in partial (50 v/v %) and total (100% v/v) replacement of mineral aggregates (river sand). Two kind of rubber particles (fine RP and coarse RG) were used in different proportion ratios to assess the influence of aggregates size on the rheological behaviour and physical, mechanical (static and dynamic), and thermo-acoustic insulation characteristics of the mixes. A comprehensive comparison with 3D-printable rubberized OPC-based composites was also conducted to critically evaluate the impact of rubber addition on the properties of the two printable binders. Based on the results achieved from this study, the following conclusions can be drawn.

1. The addition of GWTR in place of sand drastically reduced the flowability of the fresh-state alkali-activated mixes. However, with an appropriate proportion of the two granulometric fractions of GWTR, it was possible to sufficiently counteract the loss of fluidity, obtaining a printable mixture.
2. All the AAM formulations were successfully printed using large-sized nozzle (20 mm diameter) to compensate for the high intrinsic viscosity of the alkali-activated binder. Smaller nozzle orifices (10 mm and 15 mm diameters) caused nozzle's obstruction and extrudability issues.
3. For AAM mixes, proper optimization of the mixes rheology and printing process parameters were achieved. Results of unit weight and mechanical testing revealed levels of discrepancy between mold-cast and 3D-printed samples as well as mechanical anisotropy degrees significantly lower than common values reported in the literature.

4. AAM mixes behaved better in flexural than OPC composites because of the greater compatibility of GWTR with the alkali-activated binder. Amongst the fully rubberized composites, highest performance was found in RP25-RG75 mix, both for the improved crack-arresting capacity of coarse rubber aggregates and for lower water content, so preserving better microstructural and strength characteristics. The developed alkali-activated formulations satisfied the minimum ASTM flexural strength requirement (2 MPa) for structural lightweight concrete.
5. The compressive strength of OPC mixes prevailed over the AAM composites. However, the test revealed higher print quality, in terms of AD, of AAM composites with respect OPC counterparts.
6. DMTA highlighted better dynamic-mechanical performance and heat stability of alkali-activated samples compared to OPC composites, demonstrating the well-known thermo-mechanical resistance of AAM. Good interfacial adhesion between rubber and alkali-activated matrix would inhibit the energy dissipative action induced by the polymer aggregate, explaining the reduced damping capacity (tan δ) of AAM mixtures compared to OPC samples.
7. Thermal insulating performances of both OPC and AAM composites were remarkably improved with the use of GWTR as aggregates. The k-value detected were aligned with the typical values for cementitious materials commonly intended for heat insulating and energy efficiency applications in building, such as foamed or lightweight insulating concretes. At the same sand-GWTR replacement level, alkali-activated composites provided lower heat conductivity than OPC mixes.
8. Incorporating rubber aggregate into AAM improved low-frequency sound insulation properties. At high frequencies, the denser AAM provided better noise insulation performance than OPC samples.

The use of GWTR aggregates was proved to be a viable way to further enhance the eco-functionality of AAM for lightweight applications using additive manufacturing. Improving the compression strength performance is one of the primary challenges to be faced. However, it has been shown that in terms of print quality and mechanical anisotropy, AAM mixes represent a more effective solution than OPCs in the field of AM processes.

Future investigations needs be done to broaden the materials' characterization, including durability assessment, frequency sweep for DMTA, microstructural inspection, implementation of the acoustic chamber method for validation of noise insulation characteristics, and printing pattern design with the aim of extrapolating useful information for optimization of material and process.

Declaration of Competing Interest

The authors declare that they have no known competing financial interests or personal relationships that could have appeared to influence the work reported in this paper.

Acknowledgements

REFERENCES

[1] El Jazzar M, Urban H, Schranz C, Nassereddine H. Construction 4.0: a roadmap to shaping the future of construction. In: ISARC. Proceedings of the international symposium on automation and robotics in construction, 37. IAARC Publications; 2020. p. 1314–21. https://doi.org/10.22260/ISARC2020/0180.

[2] de Almeida Barbosa Franco J, Domingues AM, de Almeida Africano N, Deus RM, Battistelle RAG. Sustainability in the civil construction sector supported by industry 4.0 technologies: challenges and opportunities. Infrastructures 2022;7:43. https://doi.org/10.3390/infrastructures7030043.

[3] Ranjan R, Kumar D, Kundu M, Moi SC. A critical review on Classification of materials used in 3D printing process. Materials Today: Proceedings 2022;61:43–9. https://doi.org/10.1016/j.matpr.2022.03.308.

[4] Asprone D, Auricchio F, Menna C, Mercuri V. 3D printing of reinforced concrete elements: technology and design approach. Construct Build Mater 2018;165:218–31. https://doi.org/10.1016/j.conbuildmat.2018.01.018.

[5] Ness DA, Xing K. Toward a resource-efficient built environment: a literature review and conceptual model. J Ind Ecol 2017;21(3):572–92. https://doi.org/10.1111/jiec.12586.

[6] Buswell RA, De Silva WL, Jones SZ, Dirrenberger. 3D printing using concrete extrusion: a roadmap for research. Cement Concr Res 2018;112:37–49. https://doi.org/10.1016/j.cemconres.2018.05.006.

[7] Valente M, Sibai A, Sambucci M. Extrusion-based additive manufacturing of concrete products: revolutionizing and remodeling the construction industry. Journal of composites science 2019;3(3):88. https://doi.org/10.3390/jcs3030088.

[8] Sambucci M, Marini D, Sibai A, Valente M. Preliminary mechanical analysis of rubber-cement composites suitable for additive process construction. Journal of Composites Science 2020;4(3):120. https://doi.org/10.3390/jcs4030120.

[9] Khalil A, Wang X, Celik K. 3D printable magnesium oxide concrete: towards sustainable modern architecture. Addit Manuf 2020;33:101145. https://doi.org/10.1016/j.addma.2020.101145.

[10] Valente M, Sambucci M, Chougan M, Ghaffar SH. Reducing the emission of climate-altering substances in cementitious materials: a comparison between alkali-activated materials and Portland cement-based composites incorporating recycled tire rubber. J Clean Prod 2022;333:130013. https://doi.org/10.1016/j.jclepro.2021.130013.

[11] Raza MH, Zhong RY, Khan M. Recent advances and productivity analysis of 3D printed geopolymers. Addit Manuf 2022;52:102685. https://doi.org/10.1016/j.addma.2022.102685.

[12] Bai G, Wang L, Ma G, Sanjayan J, Bai M. 3D printing eco-friendly concrete containing under-utilised and waste solids as aggregates. Cement Concr Compos 2021;120:104037. https://doi.org/10.1016/j.cemconcomp.2021.104037.

[13] Amran M, Abdelgader HS, Onaizi AM, Fediuk R, Ozbakkaloglu T, Rashid RS, et al. 3D-printable alkali-activated concretes for building applications: a critical review. Construct Build Mater 2022;319:126126. https://doi.org/10.1016/j.conbuildmat.2021.126126.

[14] Ouellet-Plamondon C, Habert G. Life cycle assessment (LCA) of alkali-activated cements and concretes. In: Handbook of alkali-activated cements, mortars and concretes. Woodhead Publishing; 2015. p. 663–86. https://doi.org/10.1533/9781782422884.5.663.

[15] El-Seidy E, Chougan M, Sambucci M, Al-Kheetan MJ, Valente M, Ghaffar SH. Lightweight alkali-activated materials and ordinary Portland cement composites using recycled polyvinyl chloride and waste glass aggregates to fully replace natural sand. Construct Build Mater 2023;368:130399. https://doi.org/10.1016/j.conbuildmat.2023.130399.

[16] Wu Y, Lu B, Bai T, Wang H, Du F, Zhang Y, et al. Geopolymer, green alkali activated cementitious material: synthesis, applications and challenges. Construct Build Mater 2019;224:930–49. https://doi.org/10.1016/j.conbuildmat.2019.07.112.

[17] Pacheco-Torgal F, Abdollahnejad Z, Miraldo S, Kheradmand M. Alkali-activated cement-based binders (AACBs) as durable and cost-competitive low-CO2 binder materials: some shortcomings that need to be addressed. Handbook of low carbon concrete 2017:195–216. https://doi.org/10.1016/B978-0-12-804524-4.00009-9.

[18] Chen Y, Jia L, Liu C, Zhang Z, Ma L, Chen C, et al. Mechanical anisotropy evolution of 3D-printed alkali-activated materials with different GGBFS/FA combinations. J Build Eng 2022;50:104126. https://doi.org/10.1016/j.jobe.2022.104126.

[19] Yuan Q, Gao C, Huang T, Zuo S, Yao H, Zhang K, et al. Factors influencing the properties of extrusion-based 3D-printed alkali-activated fly ash-slag mortar. Materials 2022;15(5):1969. https://doi.org/10.3390/ma15051969.

[20] Sikora P, Chougan M, Cuevas K, Liebscher M, Mechtcherine V, Ghaffar SH, et al. The effects of nano-and micro-sized additives on 3D printable cementitious and alkali-activated composites: a review. Appl Nanosci 2022;12:805–23. https://doi.org/10.1007/s13204-021-01738-2.

[21] Alghamdi H, Neithalath N. Synthesis and characterization of 3D-printable geopolymeric foams for thermally efficient building envelope materials. Cement Concr Compos 2019;104:103377. https://doi.org/10.1016/j.cemconcomp.2019.103377.

[22] Xiao J, Zou S, Ding T, Duan Z, Liu Q. Fiber-reinforced mortar with 100% recycled fine aggregates: a cleaner perspective on 3D printing. J Clean Prod 2021;319:128720. https://doi.org/10.1016/j.jclepro.2021.128720.

[23] Cuevas K, Chougan M, Martin F, Ghaffar SH, Stephan D, Sikora P. 3D printable lightweight cementitious composites with incorporated waste glass aggregates and expanded microspheres—Rheological, thermal and mechanical properties. J Build Eng 2021;44:102718. https://doi.org/10.1016/j.jobe.2021.102718.

[24] Dai S, Zhu H, Zhai M, Wu Q, Yin Z, Qian H, et al. Stability of steel slag as fine aggregate and its application in 3D printing materials. Construct Build Mater 2021;299:123938. https://doi.org/10.1016/j.conbuildmat.2021.123938.

[25] Skibicki S, Pułtorak M, Kaszyńska M, Hoffmann M, Ekiert E, Sibera D. The effect of using recycled PET aggregates on mechanical and durability properties of 3D printed mortar. Construct Build Mater 2022;335:127443. https://doi.org/10.1016/j.conbuildmat.2022.127443.

[26] Dabic-Miletic S, Simic V, Karagoz S. End-of-life tire management: a critical review. Environ Sci Pollut Res 2021;28:68053–70. https://doi.org/10.1007/s11356-021-16263-6.

[27] Eldin NN, Senouci AB. Observations on rubberized concrete behavior. Cem Concr Aggregates 1993;15(1):74–84. https://www.astm.org/cca10590j.html.

[28] Qaidi SM, Dinkha YZ, Haido JH, Ali MH, Tayeh BA. Engineering properties of sustainable green concrete incorporating eco-friendly aggregate of crumb rubber: a review. J Clean Prod 2021;324:129251. https://doi.org/10.1016/j.jclepro.2021.129251.

[29] Svoboda J, Dvorský T, Václavík V, Charvát J, Máčalová K, Heviánková S, et al. Sound-absorbing and thermal-insulating properties of cement composite based on recycled rubber from waste tires. Appl Sci 2021;11(6):2725. https://doi.org/10.3390/app11062725.

[30] Youssf O, Elchalakani M, Hassanli R, Roychand R, Zhuge Y, Gravina RJ, et al. Mechanical performance and durability of geopolymer lightweight rubber concrete. J Build Eng 2022;45:103608. https://doi.org/10.1016/j.jobe.2021.103608.

[31] Qaidi SM, Mohammed AS, Ahmed HU, Faraj RH, Emad W, Tayeh BA, et al. Rubberized geopolymer composites: a comprehensive review. Ceram Int 2022;48(17):24234−59. https://doi.org/10.1016/j.ceramint.2022.06.123.

[32] Dong M, Elchalakani M, Karrech A, Yang B. Strength and durability of geopolymer concrete with high volume rubber replacement. Construct Build Mater 2021;274:121783. https://doi.org/10.1016/j.conbuildmat.2020.121783.

[33] Sambucci M, Valente M. Influence of waste tire rubber particles size on the microstructural, mechanical, and acoustic insulation properties of 3D-printable cement mortars. Civ Eng J 2021;7:937−52. https://doi.org/10.28991/cej-2021-03091701.

[34] Sambucci M, Valente M, Sibai A, Marini D, Quitadamo A, Musacchi E. Rubber-cement composites for additive manufacturing: physical, mechanical and thermo-acoustic characterization. In: Bos F, Lucas S, Wolfs R, Salet T, editors. Second RILEM international conference on concrete and digital fabrication. DC. RILEM bookseries, 28. Cham: Springer; 2020. https://doi.org/10.1007/978-3-030-49916-7_12.

[35] BS EN 450-1. Fly ash for concrete. Definition, specifications, and conformity criteria. London, UK: British Standards Institution; 2012.

[36] BS 410-1. Test sieves: technical requirements and testing − Part 1: test sieves of metal wire cloth. London, UK: British Standards Institution; 2000.

[37] DIN 66165-2. Particle size analysis—sieving analysis—Part 2: procedure. Berlin, GE: DIN German Institute for Standardization; 2016.

[38] Sukontasukkul P, Tiamlom K. Expansion under water and drying shrinkage of rubberized concrete mixed with crumb rubber with different size. Construct Build Mater 2012;29:520−6. https://doi.org/10.1016/j.conbuildmat.2011.07.032.

[39] Martínez-Barrera G, del Coz-Díaz JJ, Álvarez-Rabanal FP, Gayarre FL, Martínez-López M, Cruz-Olivares J. Waste tire rubber particles modified by gamma radiation and their use as modifiers of concrete. Case Stud Constr Mater 2020;12:e00321. https://doi.org/10.1016/j.cscm.2019.e00321.

[40] Liu W, Xu Y, Wang H, Shu B, Barbieri DM, Norambuena-Contreras J. Enhanced storage stability and rheological properties of asphalt modified by activated waste rubber powder. Materials 2021;14(10):2693. https://doi.org/10.3390/ma14102693.

[41] Albar, A, Chougan, M, Al-Kheetan, M.J, Swash, MR, Ghaffar, SH. Effective extrusion-based 3D printing system design for cementitious-based materials. Results in engineering; 6: 100135. https://doi.org/10.1016/j.rineng.2020.100135.

[42] Chougan, M, Ghaffar, S H, Jahanzat, M, Albar, A, Mujaddedi, N, Swash, R. The influence of nano-additives in strengthening mechanical performance of 3D printed multi-binder geopolymer composites. Construct Build Mater; 250: 118928. https://doi.org/10.1016/j.conbuildmat.2020.118928.

[43] BS EN 12350-5. Testing fresh concrete - flow table test. London, UK: British Standards Institution; 2009.

[44] Papachristoforou M, Mitsopoulos V, Stefanidou M. Use of by-products for partial replacement of 3D printed concrete constituents; rheology, strength and shrinkage performance. Frat Ed Integrità Strutt 2019;13(50):526−36. https://doi.org/10.3221/IGF-ESIS.50.44.

[45] Oyinloye TM, Yoon WB. Investigation of flow field, die swelling, and residual stress in 3D printing of surimi paste using the finite element method. Innovat Food Sci Emerg Technol 2022;78:103008. https://doi.org/10.1016/j.ifset.2022.103008.

[46] BS 1881-114. Method for Determination of Density of hardened concrete. London, UK: British Standards Institution; 1983.

[47] BS EN 196-1. Methods of testing cement. Determination of strength. London, UK: British Standards Institution; 2016.

[48] Rehman AU, Kim J-H. 3D concrete printing: a systematic review of rheology, mix designs, mechanical, microstructural, and durability characteristics. Materials 2021;14(14):3800. https://doi.org/10.3390/ma14143800.

[49] Neagu RC, Bourban PE, Månson JAE. Micromechanics and damping properties of composites integrating shear thickening fluids. Compos Sci Technol 2009;69(3−4):515−22. https://doi.org/10.1016/j.compscitech.2008.11.019.

[50] Damiani RM, Mondal P, Lange DA. Mechanical performance of rubberized cement paste with calcium sulfoaluminate cement addition. Construct Build Mater 2021;266:120790. https://doi.org/10.1016/j.conbuildmat.2020.120790.

[51] ASTM D7984. Standard test method for measurement of thermal effusivity of fabrics using a modified transient plane source (MTPS) instrument. West Conshohocken, Pennsylvania (PA), USA: ASTM International; 2021.

[52] El-Seidy E, Sambucci M, Chougan M, Al-Kheetan MJ, Biblioteca I, Valente M, et al. Mechanical and physical characteristics of alkali-activated mortars incorporated with recycled polyvinyl chloride and rubber aggregates. J Build Eng 2022;60:105043. https://doi.org/10.1016/j.jobe.2022.105043.

[53] Youssf O, ElGawady MA, Mills JE, Ma X. An experimental investigation of crumb rubber concrete confined by fibre reinforced polymer tubes. Construct Build Mater 2014;53:522−32. https://doi.org/10.1016/j.conbuildmat.2013.12.007.

[54] Ismail MK, Hassan AA. Influence of mixture composition and type of cementitious materials on enhancing the fresh properties and stability of self-consolidating rubberized concrete. J Mater Civ Eng 2016;28(1):04015075. https://doi.org/10.1061/(ASCE)MT.1943-5533.0001338.

[55] Chylík R, Trtík T, Fládr J, Bílý P. Mechanical properties and durability of crumb rubber concrete. In: IOP conference series: materials science and engineering, 236. IOP Publishing; 2017, 012093. https://doi.org/10.1088/1757-899X/236/1/012093. 1.

[56] Sambucci M, Marini D, Valente M. Tire recycled rubber for more eco-sustainable advanced cementitious aggregate. Recycling 2020;5(2):11. https://doi.org/10.3390/recycling5020011.

[57] Youssf O, Hassanli R, Mills JE, Skinner W, Ma X, Zhuge Y, et al. Influence of mixing procedures, rubber treatment, and fibre additives on rubcrete performance. Journal of Composites Science 2019;3(2):41. https://doi.org/10.3390/jcs3020041.

[58] Bajare D, Kazjonovs J, Korjakins A. Lightweight concrete with aggregates made by using industrial waste. J Sustain Architect Civ Eng 2013;4(5):67−73. https://doi.org/10.5755/j01.sace.4.5.4188.

[59] Aliabdo AA, Abd Elmoaty M, Salem HA. Effect of water addition, plasticizer and alkaline solution constitution on fly ash based geopolymer concrete performance. Construct

Build Mater 2016;121:694–703. https://doi.org/10.1016/j.conbuildmat.2016.06.062.

[60] ASTM C330. Standard specification for lightweight aggregates for structural concrete. West Conshohocken, Pennsylvania (PA), USA: ASTM International; 2005.

[61] Hou S, Duan Z, Xiao J, Ye J. A review of 3D printed concrete: performance requirements, testing measurements and mix design. Construct Build Mater 2021;273:121745. https://doi.org/10.1016/j.conbuildmat.2020.121745.

[62] Liu J, Li S, Gunasekara C, Fox K, Tran P. 3D-printed concrete with recycled glass: effect of glass gradation on flexural strength and microstructure. Construct Build Mater 2022;314:125561. https://doi.org/10.1016/j.conbuildmat.2021.125561.

[63] Segre N, Ostertag C, Monteiro PJM. Effect of tire rubber particles on crack propagation in cement paste. Mater Res 2006;9:311–20. https://doi.org/10.1590/S1516-14392006000300011.

[64] Xiao J, Liu H, Ding T. Finite element analysis on the anisotropic behavior of 3D printed concrete under compression and flexure. Addit Manuf 2021;39:101712. https://doi.org/10.1016/j.addma.2020.101712.

[65] Shill SK, Al-Deen S, Ashraf Mahmud. Thermal and chemical degradation of Portland cement concrete in the military airbase. In: CRIOCM 2017 : Proceedings of the 22nd international Conference on Advancement of construction Management and real estate. Melbourne, Vic: CRIOCM; 2017. p. 43–50. https://easychair.org/publications/preprint/b24Q.

[66] Song Q, Guo MZ, Ling TC. A review of elevated-temperature properties of alternative binders: supplementary cementitious materials and alkali-activated materials. Construct Build Mater 2022;341:127894. https://doi.org/10.1016/j.conbuildmat.2022.127894.

[67] Junaid MT, Khennane A, Kayali O, Sadaoui A, Picard D, Fafard M. Aspects of the deformational behaviour of alkali activated fly ash concrete at elevated temperatures. Cement Concr Res 2014;60:24–9. https://doi.org/10.1016/j.cemconres.2014.01.026.

[68] Sayahi F, Emborg M, Hedlund H. Effect of water-cement ratio on plastic shrinkage cracking in self-compacting concrete. In: 23th symposium on nordic concrete research & developement. Aalborg, Denmark: Nordic Concrete Federation; 21-23 August 2017.

[69] Gupta T, Chaudhary S, Sharma RK. Assessment of mechanical and durability properties of concrete containing waste rubber tire as fine aggregate. Construct Build Mater 2014;73:562–74. https://doi.org/10.1016/j.conbuildmat.2014.09.102.

[70] Siddika A, Al Mamun MA, Alyousef R, Amran YM, Aslani F, Alabduljabbar H. Properties and utilizations of waste tire rubber in concrete: a review. Construct Build Mater 2019;224:711–31. https://doi.org/10.1016/j.conbuildmat.2019.07.108.

[71] Chi L, Lu S, Yao Y. Damping additives used in cement-matrix composites: a review. Compos B Eng 2019;164:26–36. https://doi.org/10.1016/j.compositesb.2018.11.057.

[72] Najim KB, Hall MR. Mechanical and dynamic properties of self-compacting crumb rubber modified concrete. Construct Build Mater 2012;27(1):521–30. https://doi.org/10.1016/j.conbuildmat.2011.07.013.

[73] Ajayan PM, Suhr J, Koratkar N. Utilizing interfaces in carbon nanotube reinforced polymer composites for structural damping. J Mater Sci 2006;41(23):7824–9. https://doi.org/10.1007/s10853-006-0693-4.

[74] Wongsa A, Zaetang Y, Sata V, Chindaprasirt P. Properties of lightweight fly ash geopolymer concrete containing bottom ash as aggregates. Construct Build Mater 2016;111:637–43. https://doi.org/10.1016/j.conbuildmat.2016.02.135.

[75] Krakowiak KJ, Nannapaneni RG, Moshiri A, Phatak T, Stefaniuk D, Sadowski L, et al. Engineering of high specific strength and low thermal conductivity cementitious composites with hollow glass microspheres for high-temperature high-pressure applications. Cement Concr Compos 2020;108:103514. https://doi.org/10.1016/j.cemconcomp.2020.103514.

[76] Duxson P, Lukey GC, van Deventer JS. Thermal conductivity of metakaolin geopolymers used as a first approximation for determining gel interconnectivity. Ind Eng Chem Res 2006;45(23):7781–8. https://doi.org/10.1021/ie060187o.

[77] Adesina A. Overview of the influence of waste materials on the thermal conductivity of cementitious composites. Cleaner Engineering and Technology 2021;2:100046. https://doi.org/10.1016/j.clet.2021.100046.

[78] Chávez-Valdez A, Arizmendi-Morquecho A, Vargas G, Almanza JM, Alvarez-Quintana J. Ultra-low thermal conductivity thermal barrier coatings from recycled fly-ash cenospheres. Acta Mater 2011;59(6):2556–62. https://doi.org/10.1016/j.actamat.2011.01.011.

[79] Newman J, Choo BS. Advanced concrete technology 2: concrete properties. 1st ed. London, UK: Butterworth-Heinemann; 2003.

[80] Turgut P, Yesilata B. Physico-mechanical and thermal performances of newly developed rubber-added bricks. Energy Build 2008;40(5):679–88. https://doi.org/10.1016/j.enbuild.2007.05.002.

[81] Raj A, Sathyan D, Mini KM. Physical and functional characteristics of foam concrete: a review. Construct Build Mater 2019;221:787–99. https://doi.org/10.1016/j.conbuildmat.2019.06.052.

[82] Bala A, Gupta S. Thermal resistivity, sound absorption and vibration damping of concrete composite doped with waste tire Rubber: a review. Construct Build Mater 2021;299:123939. https://doi.org/10.1016/j.conbuildmat.2021.123939.

[83] Herrero S, Mayor P, Hernández-Olivares F. Influence of proportion and particle size gradation of rubber from end-of-life tires on mechanical, thermal and acoustic properties of plaster–rubber mortars. Mater Des 2013;47:633–42. https://doi.org/10.1016/j.matdes.2012.12.063.

[84] Kumar S, Lee HP. The present and future role of acoustic metamaterials for architectural and urban noise mitigations. Acoustics 2019;1:590–607. https://doi.org/10.3390/acoustics1030035.

[85] Sambucci M, Valente M. Ground waste tire rubber as a total replacement of natural aggregates in concrete mixes: application for lightweight paving blocks. Materials 2021;14(24):7493. https://doi.org/10.3390/ma14247493.

[86] Berglund B, Hassmén P, Job RS. Sources and effects of low-frequency noise. J Acoust Soc Am 1996;99(5):2985–3002. https://doi.org/10.1121/1.414863.

[87] Gandoman M, Kokabi M. Sound barrier properties of sustainable waste rubber/geopolymer concretes. Iran Polym J (Engl Ed) 2015;24(2):105–12. https://doi.org/10.1007/s13726-014-0304-1.

[88] Zhang B, Poon CS. Sound insulation properties of rubberized lightweight aggregate concrete. J Clean Prod 2018;172:3176–85. https://doi.org/10.1016/j.jclepro.2017.11.044.

[89] Karlinasari L, Hermawan D, Maddu A, Bagus M, Lucky IK, Nugroho N, et al. Acoustical properties of particleboards made from betung bamboo (Dendrocalamus asper) as building construction material. Bioresources 2012;7(4):5700–9. https://doi.org/10.15376/biores.7.4.5700-5709.